



National Technical University of Athens
School of Naval Architecture and Marine Engineering
Laboratory of Ship and Marine Hydrodynamics

Effect of Turbulence Modeling and roughness corrections on RANS CFD prediction of Calm Water Resistance

Diploma Thesis

Writer

Dimitrios Psalidas

Thesis Supervisor

G. Papadakis, Assistant Professor N.T.U.A.

Comittee Member: K.Anyfantis, Assistant Professor N.T.U.A.

Comittee Member: E.Aggelou, Assistant Professor N.T.U.A.

Athens, September 2023

To my mother

Abstract

The current diploma thesis was carried out as part of the studies of the writer in the school of Naval Architecture and Marine engineering of the National Technical University of Athens. The purpose of this thesis is the study of the effect of turbulence modelling in the calculation of the resistance of a ship in calm water, using RANS CFD methods. Initially, a convergence study of the computational meshes used for the calculation of the resistance coefficient was done utilizing the $k-\omega$ SST model. Then, simulations have been conducted using some variations of the original model. Finally, corrections for the hull roughness have been implemented on the original moment, and simulations to attain results regarding this case have also been realised.

Περίληψη

Η παρούσα διπλωματική εργασία εκπονήθηκε στα πλαίσια των σπουδών του συγγραφέα στη Σχολή Ναυπηγών Μηχανολόγων Μηχανικών του Εθνικού Μετσόβιου Πολυτεχνείου. Σκοπός της αποτέλεσε η μελέτη της επίδρασης της τύρβης στον υπολογισμό της αντίστασης ενός πλοίου με τη χρήση μεθόδων RANS CFD. Αρχικά πραγματοποιήθηκε μελέτη σύγκλισης των υπολογιστικών πλεγμάτων για τον υπολογισμό της αντίστασης σε ένα αραιό υπολογιστικό πλέγμα χρησιμοποιώντας το μοντέλο τύρβης $k-\omega$ SST. Στη συνέχεια εκτελέστηκαν προσομοιώσεις χρησιμοποιώντας μερικές παραλλαγές του μοντέλου $k-\omega$ SST. Τέλος, έγινε διόρθωση του μοντέλου για τις επιδράσεις της τραχύτητας στην αντίσταση, και πραγματοποιήθηκαν προσομοιώσεις και για αυτήν την περίπτωση.

Acknowledgements

This Thesis marks the end of my studies in the school of Naval Architecture and Marine Engineering. This Thesis is my first experience in the field of Computational Fluid Dynamics, an extreme learning experience for me.

First of all, I would like to thank my supervisor, professor G.Papadakis, for allowing me to have the chance of completing my studies this way, and for guiding me through all of this. I would also like to thank PhD candidate Dimitris Ntouras, for his amazing guidance throughout this experience. Helping me solving all sorts of problems, guiding me through all of this work, both professor Papadakis and candidate Ntouras have been a big part in my learning experience, and I wholeheartedly thank them for this learning experience.

I would also like to thank my family, for their everlasting support throughout these years of studying in this University. Their support is what helped me get through this very challenging experience of studying in National Technical University of Athens.

On the same wavelength, I would also like to thank all my friends, and give a special thanks to Antonis and Christina, who I met on this school. Studying with them all those years, has made me evolve academically and spiritually

The Writer,
Dimitrios Psalidas

Contents

1	Introduction	1
1.1	General	1
1.2	Thesis Scope	4
2	MaPFlow Solver	6
2.1	Navier Stokes Equations	6
2.2	Volume of Fluid Method	6
2.3	Artificial Compressibility(AC)	7
2.4	Conservative Form of the Flow Equations	7
2.5	Discretization of the Flow Equations	8
2.6	Variable Reconstruction Scheme	9
2.6.1	Piecewise linear Reconstruction(PLR)	9
2.6.2	Interface Capturing Schemes	10
2.6.3	High Resolution interface Capturing Schene(HRIC)	10
2.7	Convective and Viscous Fluxes	11
2.7.1	Convective Fluxes	11
2.8	Viscous Fluxes	11
2.9	Temporal Discretization	12
2.10	Boundary Conditions	12
2.10.1	Symmetry boundary condition	13
2.10.2	Solid Wall Boundary condition	13
2.10.3	Farfield boundary conditions	13
2.11	Numerical Wave Tank	13
2.11.1	Wave Generation and Absorbtion	14
3	Turbulence Modelling	16
3.1	Reynolds-Averaged Navier Stokes(RANS)	16

3.1.1	The Standard Menter $k-\omega$ SST (Shear Stress Transport)Model	17
3.1.2	Boundary Conditions	18
3.1.3	The $k-\omega$ SSTm Model	19
3.1.4	The $k-\omega$ SST Model with Vorticity source (SST-V)	19
3.1.5	The $k-\omega$ SST-Vm Model	19
3.1.6	The $k-\omega$ SST model with Kato-Launder source term(SST-KL, SST-Klm)	19
3.2	Boundary Layer-Law of the Wall	20
3.3	Wall Functions	21
3.3.1	Automatic Wall Treatment	21
3.4	Hull roughness and its effect on ship resistance	22
3.4.1	Wall Functions with roughness corrections	23
4	Mesh Construction	24
4.1	The HEXPRESS Software	24
4.2	Initial Mesh	24
4.3	Adapt to Geometry	25
4.4	Snap to Geometry-Optimization	26
4.5	Viscous Layers	27
4.6	Refinement boxes	27
4.7	Boundary Conditions	28
5	Results	30
5.1	Hull Geometry	30
5.2	$k - \omega$ SST simulation results	33
5.3	$k - \omega$ SSTm simulation results	37
5.4	$k - \omega$ SST - V_m simulation results	39
5.5	$k - \omega$ SST-Klm simulation results	40
5.6	Roughness correction results (hs=120 μ m)	42
5.7	Roughness correction results(hs=300 μ m)	43
5.8	Resistance Results	45

List of Figures

1.1	Built hull model	1
1.2	Simulation of fluid flow around a hull	2
1.3	Laminar and Turbulent flow	3
2.1	Configuration of variable reconstruction	9
3.1	Normalised mean velocity profile in a turbulent boundary layer in semi-log coordinates	20
3.2	Fully Resolved boundary Layer and Wall function Theory	21
3.3	fouled hull	22
3.4	effect of sand grains on the velocity profile in a pipe	23
4.1	The HEXPRESS algorithm	24
4.2	Initial mesh of 100.000 cells	25
4.3	cell refinement	25
4.4	cell Trimming	26
4.5	Hull surface mesh	26
4.6	Mesh around the hull	26
4.7	Viscous Layers	27
4.8	Mesh around the hull after Viscous Layer insertion	27
4.9	Cut plane on the Trim height-Refinement for the Kelvin Wake Pattern	28
5.1	The Kriso Container Ship	31
5.2	Force on X-Axis(Resistance)-Time iterations	32
5.3	Wave Elevation- $k-\omega$ SST model	33
5.4	Wave elevation close to the hull	33
5.5	Wave elevation on Hull surface-MaPFlow and Experiment	34
5.6	Wave cut $y/L-0.0741$ -MaPFlow and Experiment	34
5.7	Wave cut $y/L-1509$ -MaPFlow and Experiment	35

5.8	y-z Velocity contour	36
5.9	Mean Axial Velocity Contour	36
5.10	Wave Elevation-k- ω SSTm model	37
5.11	Wave elevation close to the hull	37
5.12	y-z Velocity contour	38
5.13	Mean Axial Velocity Contour	38
5.14	Wave Elevation-k- ω SST Vm model	39
5.15	Wave elevation close to hull: k- ω SSTm(left) and SST-Vm(right) . .	39
5.16	y-z Velocity Contour	39
5.17	Mean Axial Velocity Contour	40
5.18	Wave Elevation-k- ω SST-KLm model	40
5.19	Wave elevation close to hull:k- ω SST-Vm(left) and SST-KLm(right)	40
5.20	y-z Velocity Contour	41
5.21	Mean Axial Velocity Contour	41
5.22	Wave Elevation:k- ω SST model With roughness correction($h_s =$ $120\mu m$	42
5.23	Wave elevation close to hullk- ω SST model Without roughness correction(left)- With roughness correction(right)	42
5.24	y-z Velocity Contour	42
5.25	Mean Axial Velocity Contour	43
5.26	Wave Elevation:k- ω SST model With roughness correction($h_s =$ $300\mu m$	43
5.27	Wave Elevation close to hull: $h_s = 120\mu m$ (left) $h_s = 300\mu m$ (right) .	44
5.28	y-z Velocity Contour	44
5.29	Mean Axial Velocity Contour	44

List of Tables

5.1.1	Hull Geometry	30
5.1.2	Mesh convergence	32
5.8.1	comparison of the resistance coefficients of the simulations	45

Chapter 1

Introduction

1.1 General

The resistance of ships has always been a major topic of interest in the science of naval architecture and marine engineering. It plays a very important part in the ship engine selection, propeller selection, and also on the hydrodynamic frames of the ship.

Even more research has been conducted on finding ways to deduce the resistance of a ship for a given operational velocity. Reducing the resistance is important for both economic, engineering, and environmental reasons. Selection of appropriate engine motors used in order to produce the necessary thrust to overcome the ship's resistance is one of the main parameters of marine engineering, combined with the ideal propeller selection, in order to produce a functioning engine-propeller combination, and this combination is inextricably linked to the ship resistance. It is also an important factor in economic management. Depending on the engine, a corresponding fuel is used, which also takes economic resources from the ship operator.

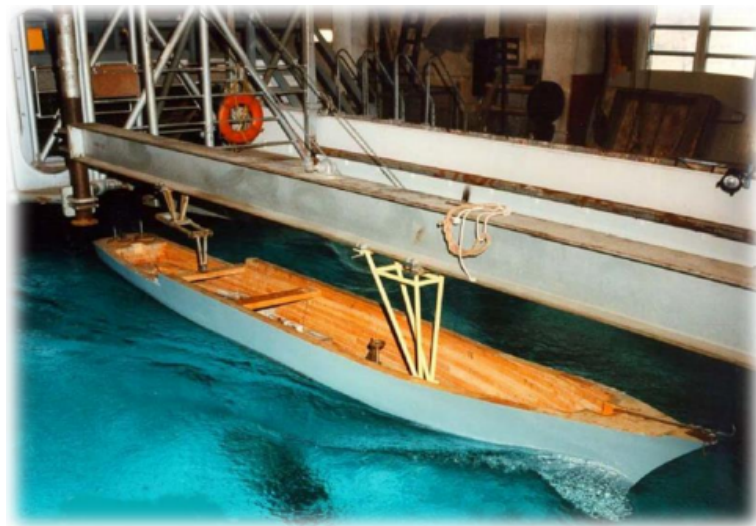


Figure 1.1: Built hull model

For all the above reasons, finding the resistance of a ship, is important and essential. Over the years of marine hydrodynamics, there have been various methods developed in order to accomplish this task. This task is directly related to fluid flow problems, and as the science of fluid dynamics developed, the quest to find an accurate value

for the resistance of a ship became much easier. The most common methods used were experimental methods. A model of the ship was created in a geometric scale, and experiments were conducted on it in order to measure the resistance.

Using dimensional analysis theories, it became possible for researchers to extract a value for the resistance of the real ship, based on the experimental results. These methods were widely used for many years. However, with the evolution of computer technology, new methods to obtain results have emerged, in the form of Computational Fluid Dynamics(CFD).

Computational Fluid Dynamics, utilising numerical methods and the computational strength of computers to solve the non-linear partial differential equations of the fluid flow problem. Over the last centuries, these methods took over experiments in many fields. The increase in computational resources and computer strength, allows for even better simulation conditions, with faster result extraction. In marine hydrodynamics, experimental and computational methods are utilized for various cases, and comparison between the two are often conducted. In the case of the ship resistance problem, both methods are used quite frequently. CFD simulations can be especially good at providing an accurate result for the fluid flow around the hull, or any floating body. The CFD method used in this study is the Finite Volume Method(FVM), in which the computational domain is separated into finite volume cells and the model equations are solved in their conservative form for the flow entering and exiting the volume cell. Other common methods include the Finite Difference Method, solving the system of differential equations of the model, by approximating derivatives with finite differences. The Finite Element Method, is also very commonly used, and the problem is approached by separating the flow field into smaller elements(such as triangles or squares), and distributing the variables on every element, solving the equations for the corresponding element.

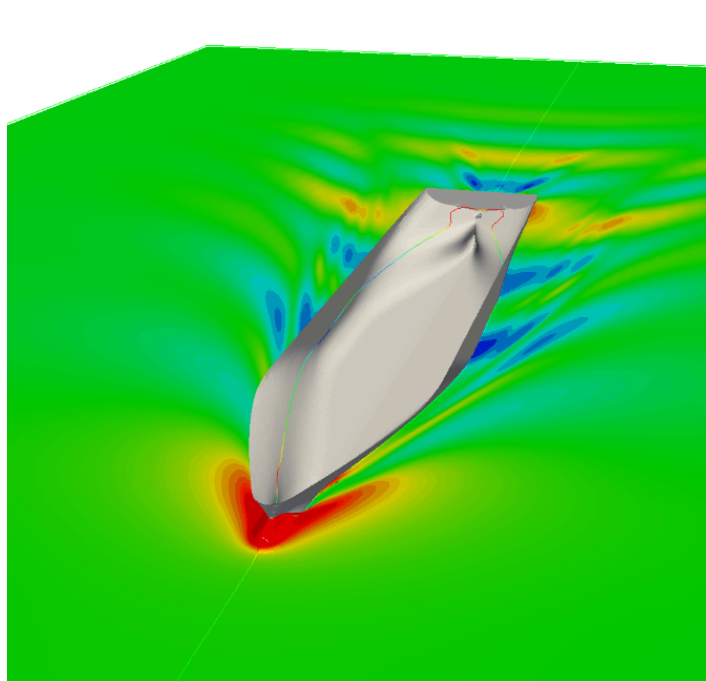


Figure 1.2: Simulation of fluid flow around a hull

Computational Fluid dynamics also come with their share of challenges. As the

simulation quality relies heavily on the computational mesh, the complexity of the geometry of the flow problem can make requirements for much bigger meshes, thus increasing computational cost. Even in less complex cases, CFD simulations require lots of computational resources. This problem is usually solved distributing the computational weight across multiple computers, which in turn requires more resources. Also, depending on the problem, a different model of approach needs to be set up and used, as different models can give different results in different problems.

The study of fluid Dynamics resulted in 2 distinct categories of fluid flow. The first one, the laminar flow, also called streamline flow is a type of flow where the fluid particles travel in smooth paths parallel to each other, with minimal amount of mixing between them. As the velocity of the fluid increases, the streamlines change a lot, and a much more complex flow regime emerges, the turbulent flows.

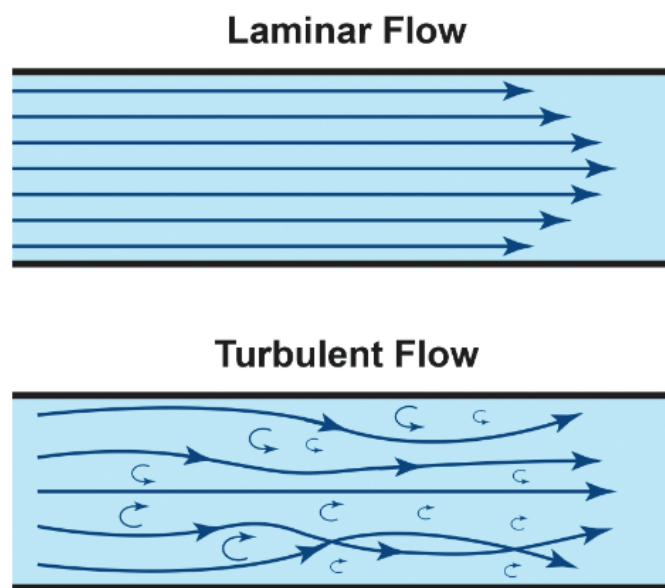


Figure 1.3: Laminar and Turbulent flow

In turbulent flows, the fluid during the motion undergoes irregular fluctuations. Turbulent flows are characterised by chaotic movement of particles and contains swirling regions (eddies), that result in mixing between the layers. Random velocity fluctuations are in every point of the fluid motion, and this makes the turbulent flow much more difficult to analyse and model. The Reynolds number, a non-dimensional parameter consisting by the ratio of inertia to viscous forces developed by shear due to the viscosity of the fluid. introduced by Osborne Reynolds, is commonly used to distinguish between laminar and turbulent flows. On low Reynolds numbers, the viscous forces dominate, damping disturbances and the flow becomes laminar. In higher Reynolds numbers, the inertia forces dominate, resulting in turbulence fluctuations and the flow becomes turbulent.

Most flows in real world problems are turbulent, Especially in the case of a moving ship, where in most cases the flow around the hull is considered fully turbulent. Thus the need for a solution on the problem of turbulence has risen, and the field of turbulence modelling emerged. Turbulence models are mathematical equations created in order to model the turbulent behavior of the fluid, so numerical simulations can provide

accurate results for turbulent flow problems. Different categories of turbulence modelling vary in complexity and applicability. The Reynolds-Averaged Navier Stokes (RANS) models are a characteristic example that will also be considered in this thesis, with the main principle of time-averaging the turbulent flow variables, and reducing the computational cost. Other categories include the Large Eddy Simulation (LES) models, using high-resolution grids on large eddies and utilising turbulence models on smaller ones or the Dynamic Numerical Simulation (DNS), where the fluid flow equations are solved without any additional modeling with great accuracy but much higher computational cost, due to the requirement for a much finer grid resolution.

Turbulence modelling however, comes with inherent difficulties. For starters, due to the complexity of turbulence itself, turbulence models end up varying in complexity themselves. One equation, two, three and even seven equation models have been developed, in order to properly resolve the turbulence problem on a given application.

Secondly, due to the nature of turbulence, the models themselves are approximation, and come with uncertainty that can severely impact the results. Deviating from the nature of turbulence on a given fluid flow problem can yield very severe problems in the accuracy of the results, even in the case of very advanced models. Computational resources are also a problem, as turbulence modeling requires low time and space distributions to achieve accurate results.

Modeling turbulence increases computational cost, and this also needs to be taken into account. Choosing the correct turbulence model to use on a given application is also a very important task, as different turbulence models can give more accurate results on different fluid flow applications.

One of the most prevalent turbulence models used, is the two-equation Shear Stress Transport model $k-\omega$ SST, developed by Menter [12] as a blending of the previously used two-equation $k-\epsilon$ and $k-\omega$ models. This model is widely used, and some CFD solvers as the default turbulence model. Variations of the $k-\omega$ SST model are also common, and are used in different applications, such as hypersonic flow applications.

1.2 Thesis Scope

The purpose of this thesis, is to make a first comparison of the turbulence variation results in the problem of ship resistance. Specifically for the $k-\omega$ SST model, the variation of the production term of turbulence will be altered to match different variations of the original model, in order to examine how the difference in turbulence production will affect the total resistance. For the near-wall mesh wall functions will be utilised.

In this thesis, only coarse mesh results will be considered, as they can give a first impression of differences and similarities in the results. Initially, a convergence study of the resistance coefficient will be done, increasing the size of the mesh on every iteration. The resistance coefficient and free surface elevation will be compared to the respective experimental results.

After mesh convergence, the different variations of the turbulence model, shall be examined in different simulations. The results will be examined and compared with the experimental results. The aim of this comparison is to deduce if the production term variation will affect the resistance results, and thus which one of the variations is closer to the experimental results. So, if there is significant difference between them, a choice can be made, as to which variation a researcher can use to achieve better accuracy when

calculating the resistance of a ship using CFD and turbulence modelling.

Finally, a correction of the standard wall function model for hull surface roughness, will be considered, for further study of how roughness will affect the results utilising a standard roughness value. Surface roughness known for its effect on friction forces, and the fluid forces on the hull are no exceptions to this. Combining the standard $k-\omega$ SST model with the roughness corrected wall functions model will provide results comparable with the other simulations, for examination of the effects of roughness on resistance.

The hull used for the simulations is the Kriso Container Ship (KCS)[2], specifically the model built by MOERI on a scale of 31.6. The CFD solver utilised for this thesis was MaPFlow, developed by professor G. Papadakis.

Chapter 2

MaPFlow Solver

For the purpose of this thesis, the MaPFlow solver, developed by the Laboratory of ship and Maritime Hydrodynamics of N.T.U.A., was used. In this chapter, the models and formulations that were used by the solver, are briefly explained.

2.1 Navier Stokes Equations

The governing laws of mechanics, namely the conservation of mass, momentum and energy, when applied to fluid flows, give a set of partial differential equations, that are the basis of the flow problem. Assuming an in-compressible flow, and defining the velocity vector $\vec{u}(x, t) = [u, v, w]^T$, g the acceleration of gravity, ρ the fluid density, \vec{F}_B the source terms and body forces, and the stress tensor, the governing equations get the following expressions, also called Navier Stokes equations[20].

- $\nabla \cdot \vec{u} = 0$, also known as the continuity equation
- $\frac{\partial(\rho \vec{u})}{\partial t} + \rho \vec{u} \nabla \vec{u} = \rho g + \nabla \cdot \vec{\sigma} + \vec{F}_B$, the momentum equation, also known as Newton's Second Law of Motion.

2.2 Volume of Fluid Method

The flows under consideration in most hull resistance problems, are unsteady two phase flows, so the need to model the free surface is required. In this case the Volume of Fluid method (VOF)[7] is utilised.

An indicator function called the volume fraction is used in order to denote whether the phase of the fluid in the cell under consideration is liquid or gas. Using the index symbols of w for water, α for air and m for the cell under consideration, the volume fraction is defined as:

$$\alpha = \frac{\rho_m - \rho_\alpha}{\rho_w - \rho_\alpha}$$

Thus, the density and dynamic viscosity of the fluid are redefined accordingly:

$$\begin{aligned}\rho_m &= \alpha \rho_w + (1 - \alpha) \rho_\alpha \\ \mu_m &= \alpha \mu_w + (1 - \alpha) \mu_\alpha\end{aligned}$$

As the free surface is considered a material surface, the substantial derivative of the volume fraction will be 0, and thus an additional equation is derived:

$$\frac{D\alpha}{Dt} = \frac{\partial\alpha}{\partial t} + \vec{u}\nabla\alpha = 0$$

2.3 Artificial Compressibility(AC)

Applying the RANS equations on an incompressible flow has problems, as the continuity and momentum equations are decoupled, and need to be linked somehow. There are many methods to do this, but here, an Artificial Compressibility method [5] is used. The basic principle of the AC method is to use a relation between density and pressure similar to the definition of the speed of sound in a compressible fluid, using a pseudo-time derivative:

$$\frac{\partial p}{\partial \rho_\tau} = \frac{1}{\beta}$$

Now, the continuity equation is changed to

$$\frac{1}{\beta} \frac{\partial p}{\partial \tau} + \rho \nabla \vec{u} = 0$$

During convergence, the pseudo-time derivative term equals to zero, and initial equation is acquired.

2.4 Conservative Form of the Flow Equations

Having under consideration the Artificial Compressibility, we already obtained the form of the continuity equation.

$$\frac{1}{\beta} \frac{\partial p}{\partial \tau} + \rho \nabla \vec{u} = 0$$

Now, a pseudo-time derivative is also added on the momentum equation:

$$\frac{\partial(\rho\vec{u})}{\partial t} = \rho \frac{\partial\vec{u}}{\partial t} + \vec{u} \frac{\partial\rho}{\partial t} = \rho \frac{\partial\vec{u}}{\partial t} + \vec{u} \Delta\rho \frac{\partial\alpha}{\partial t}$$

Similarly, the pseudo-time derivative term becomes:

$$\frac{\partial(\rho\vec{u})}{\partial \tau} = \rho \frac{\partial\vec{u}}{\partial \tau} + \vec{u} \frac{\partial\rho}{\partial \tau} = \rho \frac{\partial\vec{u}}{\partial \tau} + \vec{u} \Delta\rho \frac{\partial\alpha}{\partial \tau}$$

Finally, the transport equation of the Volume Fraction is modified:

$$\frac{\partial\alpha}{\partial t} + \frac{\partial\alpha}{\partial \tau} + \frac{\alpha}{\rho_m\beta} \frac{\partial p}{\partial \tau} + \nabla(\vec{u}\alpha) = 0$$

The momentum, continuity, and Volume fraction equations, now form a fully coupled system of non-linear partial differential equations describing unsteady two-phase flows.

2.5 Discretization of the Flow Equations

Finite Volume Method

The discretization of the equations is done using the finite volume method. In every computational cell, a control volume is defined, with the cell center as its center. For every flow quantity Q , the spatial average over the computational cell is considered:

$$\overline{Q}_i = \frac{1}{\Omega_i} \int_{\Omega_i} \vec{Q}(x; t) d\Omega$$

Thus, integrating over the control volume in the momentum equation in the i^{th} computational cell results in the following equation:

$$\Gamma \Omega_i \frac{\partial \overline{Q}_i}{\partial \tau} + \Gamma_e \frac{\overline{Q}_i \Omega_i}{\partial \tau} = -\vec{R}_i \quad (2.5.1)$$

where:

$$\Gamma = \begin{bmatrix} \frac{1}{\beta \rho_m} & 0 & 0 \\ 0 & \rho_m I & 0 \\ \frac{\alpha_l}{\beta \rho_m} & 0 & 1 \end{bmatrix} \quad \& \quad \Gamma_e = \begin{bmatrix} 0 & 0 & 0 \\ 0 & \rho_m I & \vec{u} \Delta \rho \\ 0 & 0 & 1 \end{bmatrix}$$

the term \vec{R}_i is the spatial residual of the equations, containing the integrals of the convective and viscous fluxes obtained by the green-Gauss Theorem and the volume integral of the source terms S

$$\vec{R}_i = \oint_{\Omega_i} (\vec{F}_c - \vec{F}_v) dS - \int_{\Omega_i} S d\Omega \quad (2.5.2)$$

The bar symbol of averaging is removed and is now considered alongside the vector symbol for spacial averaging.

The convective and viscous fluxes are calculated as follows:

$$\vec{F}_c = \begin{bmatrix} V_n \\ \rho_m u \Delta V + p n_x \\ \rho_m u \Delta V + p n_y \\ \rho_m u \Delta V + p n_z \\ a_l V_n \end{bmatrix} \quad \vec{F}_v = \begin{bmatrix} 0 \\ t_{xx} n_x + t_{xy} n_{xy} + t_{xz} n_z \\ t_{yx} n_x + t_{yy} n_{yy} + t_{yz} n_z \\ t_{zx} n_x + t_{zy} n_{zy} + t_{zz} n_z \\ 0 \end{bmatrix} \quad (2.5.3)$$

where $\Delta V = V_n - V_s$, $V_n = \vec{u} \cdot \vec{n}$, $V_g = \vec{u}_{vol} \cdot \vec{n}_{vol}$ refers to the velocity of the control volume and \vec{n} denotes the surface normal to the control volume. The viscous stresses τ_{ij} will be discussed in later chapters.

Moving forwards with discretization the term \vec{R}_i is evaluated for a control volume Ω_i with N number of edges:

$$\vec{R}_i = \sum_{n=1}^N (\vec{F}_c - \vec{F}_v)_n \Delta S_n - \Omega_i \vec{S}_i \quad (2.5.4)$$

2.6 Variable Reconstruction Scheme

As said before, MaPFlow is a cell-centered code, meaning that the values of the flow variables are calculated at the centers of the cells. However, the flow variables need to be defined in the cell faces as well, in order to calculate the fluxes. This process, which is usually done via extrapolation, and is called variable reconstruction. There are several schemes for this process. In order to understand this, consider 2 adjacent cells i, j with control Volumes Ω_i, Ω_j , that are in contact with the face f . The value of vector $\vec{\phi}_i$ on the left side of f is denoted by $\vec{\phi}_L$, and on the right side as $\vec{\phi}_R$ (from $\vec{\phi}_j$)

The values of and are calculated using different schemes regarding the domain. Away from the free surface, a piecewise linear reconstruction scheme (PLR) is used for the volume fraction, which is discontinuous by definition, and in the free surface a more detailed interface capturing scheme, the HRIC scheme, is used.

2.6.1 Piecewise linear Reconstruction (PLR)

The PLR scheme, assumes that the flow variables are linearly distributed over the control volume. Thus the values of the variables in the faces, are calculated as follows:

$$\vec{\phi}_L = \vec{\phi}_i + \Psi \nabla(\phi_i \cdot \phi_j) \quad (2.6.1)$$

$$\vec{\phi}_R = \vec{\phi}_j + \Psi \nabla(\phi_i \cdot \phi_j) \quad (2.6.2)$$

Ψ is a limiter that is applied in the case of very large gradients.

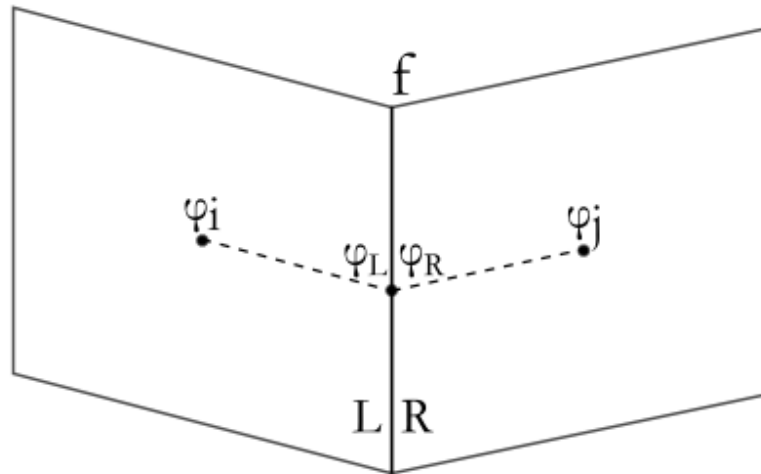


Figure 2.1: Configuration of variable reconstruction

2.6.2 Interface Capturing Schemes

The principle behind the interface capturing schemes, is the use of a blending function between a compressible and a High-Resolution advection scheme. The usage of this function depends on the angle between the flow direction and the grid lines, calculated from the gradient of ϕ and the grid orientation at the face under consideration:

$$\theta_f = \arccos \left| \frac{\nabla \phi_f \cdot \vec{n}_{ij}}{\|\nabla \phi_f\| \|\vec{n}_{ij}\|} \right| \quad (2.6.3)$$

A common feature in all these schemes is the use of the Normalised Variable Diagram [10], according to which, a variable ϕ is normalised as

$$\phi = \frac{\phi - \phi_U}{\phi_D - \phi_U} \quad (2.6.4)$$

where ϕ_U, ϕ_D demote upwind and downwind and are chosen according to the flow direction. The value of the normalised variable will be obtained using a blending function $f(\theta)$ switching between the chosen extreme schemes

$$\tilde{\phi}_f = f(\theta_f) \cdot \tilde{\phi}_{f(comp)} + [1 - f(\theta_f)] \tilde{\phi}_{f(HR)} \quad (2.6.5)$$

The schemes differ based on the choice of blending function. Below we will analyse only the scheme chosen for this particular work.

2.6.3 High Resolution interface Capturing Scheme(HRIC)

This scheme was introduced by Muzaferija [15]. Its basic principle is a blending of the Bounded Downwind and Upwind Differencing schemes, using a blending function:

$$f(\theta_f) = \sqrt{\cos(\theta_f)} \quad (2.6.6)$$

The normalised variable is given as follows:

$$\tilde{\phi}(HRIC) = \sqrt{\cos(\theta_f)} \tilde{\phi}_f(BD) + [1 - \sqrt{\cos(\theta_f)}] \tilde{\phi}_f(UD) \quad (2.6.7)$$

where $\phi_f(UD) = \phi_C$ and

$$\phi_f(BD) = \begin{cases} 2\phi_c & 0 \leq x \leq 0.5 \\ 1 & 0.5 \leq x \leq 1.0 \\ \phi_c & otherwise \end{cases}$$

The scheme is also modified with respect to the local CFL number on the edge f , defined as

$$CFL_f = \frac{\vec{u}_f \cdot S_f \Delta t}{V_f} \quad (2.6.8)$$

For CFL values lower than 0.3, there are no modifications. For CFL values higher than 0.7, the unwind scheme is used. For in-between values, the scheme is blended with the upwind scheme as follows:

$$\tilde{\phi}_f(HRIC) = \tilde{\phi}_f + [\tilde{\phi}_f - \tilde{\phi}_f(UD)] \frac{0.7 - CFL_f}{0.7 - 0.3} \quad (2.6.9)$$

2.7 Convective and Viscous Fluxes

2.7.1 Convective Fluxes

After the variable reconstruction on the faces, the problem of a discontinuity arises, due to two different values of flow variable \vec{Q}_L and \vec{Q}_R on the same face. This problem has been addressed as a Riemann problem, and is overcome using the approximate Riemann Solver of Roe[19], alongside the preconditioning matrix Γ . The jacobian that transforms the conservative variables to primitive is given as

$$A_C = \frac{\partial \vec{F}_C}{\partial \vec{Q}} = \Gamma \tilde{A}_C \quad (2.7.1)$$

$$\tilde{A}_C = \begin{bmatrix} 0 & n_x & n_y & n_z & 0 \\ n_x & \rho_m(n_x u + \Delta V) & \rho_m n_y u & \rho_m n_z & u \Delta V \Delta \rho \\ n_y & \rho_m n_x v & \rho_m(n_y u + \Delta V) & \rho_m n_z & v \Delta V \Delta \rho \\ n_z & \rho_m n_x w & \rho_m n_y w & \rho_m(n_z u + \Delta V) & w \Delta V \Delta \rho \\ 0 & \alpha_l n_x & \alpha_l n_y & \alpha_l n_z & \Delta V \end{bmatrix} \quad (2.7.2)$$

The Riemann solver provides convective flux on a face f:

$$\vec{F}_{C,f} = \frac{1}{2}(\vec{F}_C(\vec{Q}_L) + \vec{F}_C(\vec{Q}_R)) - \frac{1}{2} \overline{\Gamma |A_C|_f}(\vec{Q}_R) - \vec{F}_C(\vec{Q}_L) \quad (2.7.3)$$

where $|\tilde{A}_C| = \tilde{R}^{-1} |\tilde{\Lambda}| \tilde{R}$ is the Roe averaged preconditioned jacobian and $\tilde{R}, \tilde{R}^{-1}, \tilde{\Lambda}$ are the right, left eigenvectors and eigenvalues of the matrix, respectively. The Jacobian is determined using the Roe averaging of the flow quantities, which follow

$$\chi = \sqrt{\frac{\rho_R}{\rho_L}} \quad (2.7.4)$$

$$\tilde{\rho} = \chi \rho_L \quad (2.7.5)$$

$$\tilde{u}^i = \frac{u_L^i + \chi u_R^i}{1 + \chi}, i = 1, 2, 3 \quad (2.7.6)$$

2.8 Viscous Fluxes

The evaluation of the viscous fluxes on a face f is done via a simple averaging with the neighbour cell j

For a flow variable:

$$\vec{Q}_{ij} = \frac{1}{2}(\vec{Q}_i + \vec{Q}_j) \quad (2.8.1)$$

And for a gradient:

$$\nabla \vec{Q}_{ij} = \overline{\nabla \vec{Q}_{ij}} - [\overline{\nabla \vec{Q}_{ij}} \cdot \tau_{ij} - (\frac{\partial \vec{Q}}{\partial l})_{ij} \cdot \tau_{ij}] \quad (2.8.2)$$

where τ_{ij} is the unit vector pointing from cell i to cell j, l_{ij} is the distance between the 2 cells and $\overline{\nabla \vec{Q}_{ij}} = \frac{1}{2}(\nabla \vec{Q}_i + \nabla \vec{Q}_j)$ is the mean gradient.

2.9 Temporal Discretization

The governing equations are now discretized in the time scale. Let \vec{Q}^* be the unknown flow variables:

$$\Gamma \frac{\partial(\vec{Q}^* \Omega)}{\partial \tau} + \vec{R}^* = 0 \quad (2.9.1)$$

where \vec{R}^* is the unsteady residual, containing both the unsteady terms and the spatial residual

$$\vec{R}^* = \vec{R}_\Omega(\vec{Q}^*) + \Gamma_e \frac{\partial(\vec{Q}^* \Omega)}{\partial t} \quad (2.9.2)$$

2 indices n and k are introduced to describe the physical time stepping and pseudo-time stepping, respectively. For every physical time step, a pseudo-steady problem is solved, initializing k=0, and the flow variables are also initialised based on the previous converging solution n, so that $\vec{Q}_0^{*,n+1} = \vec{Q}_k^{*,n}$. Upon convergence the term $\Gamma \frac{\partial(\vec{Q}^* \Omega)}{\partial \tau}$ is eliminated, and the original equations reemerge.

A Backward Differentiation Formula is used for the discretization of the unsteady term:

$$\frac{\partial(\vec{Q}^* \Omega)}{\partial t} = \frac{1}{\Delta t} (\phi_{n+1}(\Omega_i \vec{Q})^{n+1} + \phi_n(\Omega_i \vec{Q})^n + \phi_{n-1}(\Omega_i \vec{Q})^{n-1} + \dots) \quad (2.9.3)$$

The pseudo-time term is discretized using a first-order backwards scheme:

$$\frac{\partial(\vec{Q}^* \Omega)}{\partial \tau} = \Omega_i^{n+1} \frac{\vec{Q}^{*,n+1} - \vec{Q}^{*,n}}{\Delta \tau} \quad (2.9.4)$$

To ensure the local convergence the local time stepping technique is used. At each computational cell i the pseudo-time step is determined by

$$\Delta \tau_i = CFL \frac{\Omega_i}{\hat{\Lambda}_{c,i}} \quad (2.9.5)$$

where $\hat{\Lambda}_{c,i} = \sum_{j=1}^{N_f} (|V_n - \frac{V_g}{2}|_c) \Delta S_{ij}$ is the convective spatial radii.

2.10 Boundary Conditions

Implementing the correct boundary conditions is crucial to the solution of any CFD problem. Different boundary conditions can give completely different results on a similar problems, and thus need to be placed correctly in order to achieve the correct results. For the two-phase flow around a hull, the boundary conditions used are:

- symmetry boundary condition
- Solid wall boundary condition
- Farfield Boundary condition

2.10.1 Symmetry boundary condition

In the case of a symmetric problem around a plane, such as the case of a flow around a ship hull, there is no need for the solution around the entire domain. The symmetry of the problem around the plane ensures that the solution on one side mirrors the other side perfectly. As such, in the case of a hull, only half the hull geometry is needed, and only the computational domain on one side is created. In order to include this property in the solution, corresponding boundary conditions need to be put on the cells on the plane of symmetry, in our case on the x-z plane, as the hull is symmetric around the y-z plane. These conditions include:

- there is no flux on the symmetry plane
- any gradients normal to the symmetry plane are zero

Mathematically, these conditions take the following form:

$$\vec{u} \cdot \vec{n} = 0 \quad (2.10.1)$$

$$\nabla \vec{u} \cdot \vec{n} = 0 \quad (2.10.2)$$

2.10.2 Solid Wall Boundary condition

In the case of a wall in the problem, such as the hull, we can consider 2 cases: the cases of inviscid wall the case of viscous wall.

In the case of an inviscid wall, due to the absence of friction, the velocity normal to the wall must be 0, and thus the velocity of the fluid is tangent to the wall. Mathematically:

$$(\vec{u} - \vec{u}_g) \cdot \vec{n} = 0 \quad (2.10.3)$$

Where \vec{u}_g denotes the mesh velocity. The pressure of the wall takes the value of the cell next to the wall.

In the case of a viscous wall, the boundary condition changes, because tangency is not needed. This condition is called no-slip boundary condition, and it requires the velocity of the surface to be the same as the velocity of the fluid:

$$\vec{u} = \vec{u}_g \quad (2.10.4)$$

2.10.3 Farfield boundary conditions

The edges of the computational domain, which are in a large enough distance from the hull, are called the far field. The major requirement for the farfield, is that no disturbances should be deflected back to the computational domain.

2.11 Numerical Wave Tank

The Numerical Wave Tank is a numerical tool that emulates the a physical wave tank. Its usage is very effective and in two-phase flow simulations, such as free-surface flows, or interaction with floating bodies. The general idea is to use certain areas of the flow, close to the boundary, where waves are generated, and absorbed, while the rest of the domain is the main point of interest. In this work though, only the radiation of the waves due to the ship is considered.

2.11.1 Wave Generation and Absorbtion

When considering a numerical Wave tank, both the generation of the desired wave profile and the radiation of the waves outside the domain are two very important tasks. The generation of a wave profile, is usually accomplished by forcing the numerical solution to follow a wave solution in a certain part of the computational domain.[3] Moreover, an artificial damping of the wave is required near the boundary of the domain as the boundary conditions assume a uniform field, thus any disturbance should not reach the boundary. Both the wave generation and absorption are accomplished by adding a source term to the momentum equation, in certain parts of the computational domain near the farfield. The source term is of the following form :

$$S_{wnt} = C_{wnt}\rho(\vec{\phi} - \vec{\phi tar}) \quad (2.11.1)$$

In this equation $\vec{\phi}$ stands for flow variables(\vec{u} velocity , pressure p, volume fraction α , and $\vec{\phi tar}$ stands for the values that the flow variables are driven to depending on the cases of wave damping or wave generation[17]. The flow variable choice is case dependant. The effect of the source term is regulated by the C_{wnt} function, which is given by the following equation:

$$C_{wnt} = \alpha \frac{\exp(x_r^n) - \exp(1)}{\exp(1) - 1}, \quad (2.11.2)$$

where x_r is a non-dimensional space variable, depending on the starting position x_s of the specified zone and the ending position x_e

$$x_r = \frac{x_s - x}{x_s - x_e} \quad (2.11.3)$$

The parameter α regulates the maximum value of the function, and n regulates its spacial distribution. The maximum value is reached in the inner boundaries of the domain, and the minimum value of zero is acquired at the end of each specified zone.

Chapter 3

Turbulence Modelling

3.1 Reynolds-Averaged Navier Stokes(RANS)

RANS models are a common set of equations used in CFD. They are time-averaged versions of the Navier-Stokes equations discussed in Chapter 2. The development of the RANS equation is based on the Reynolds decomposition. According to the Reynolds decomposition, any flow variable $f(x,t)$ can be separated into 2 parts: the mean component \bar{f} and the fluctuating term f' . The mean operator is a Reynolds operator, defined as

$$\bar{f} = \frac{1}{T} \int_{t_0}^{t_0+T} f(x, t) dt \quad (3.1.1)$$

where T is a chosen time depending on the behavior of the variable.

The Reynolds mean operator obeys the following rules:

$$\overline{\bar{f}} = \bar{f} \quad (3.1.2)$$

$$\overline{f + g} = \bar{f} + \bar{g} \quad (3.1.3)$$

$$\frac{\partial \bar{f}}{\partial x} = \overline{\frac{\partial f}{\partial x}} \quad (3.1.4)$$

$$\frac{\partial \bar{f}}{\partial t} = \overline{\frac{\partial f}{\partial t}} \quad (3.1.5)$$

Also, for the fluctuating component, obviously $\overline{f'} = 0$

Applying these properties into the initial Navier Stokes equations, we get the following:

$$\frac{\partial \bar{u}_i}{\partial x_i} = 0 \quad (3.1.6)$$

$$\frac{\partial \bar{u}_i}{\partial t} + \bar{u}_j \frac{\partial \bar{u}_i}{\partial x_j} = \rho f_i + \frac{\partial}{\partial x_j} (-p_{ij} + 2S_{ij} - \overline{u'v'}) \quad (3.1.7)$$

where $S_{ij} = \frac{1}{2} \left(\frac{\partial \bar{u}_i}{\partial x_j} + \frac{\partial \bar{u}_j}{\partial x_i} \right)$

the term $\overline{u'v'}$ is known as the Reynolds stress τ_{ij} which is the term that needs to be provided by the turbulence models. The model this thesis will focus on and apply is the two equation k- ω SST Model and its different variations.

3.1.1 The Standard Menter k- ω SST (Shear Stress Transport)Model

This model is a two equation viscosity eddy model combining the traditional k- ϵ and k- ω models. The traditional k- ω model has excellent behaviour in near-wall treatment-while the k- ϵ model has very good accuracy in the free stream turbulent properties. A blending of these 2 models gives us the following 2 equations for the turbulent kinetic energy k and dissipation rate ω :

$$\frac{\partial \rho k}{\partial t} + \frac{\partial(\rho u_i k)}{\partial x_j} = P - \beta \cdot \rho \omega k + \frac{\partial}{\partial x_j} (\mu + \sigma_k \mu_t \frac{\partial k}{\partial x_j}) \quad (3.1.8)$$

$$\frac{\partial \rho \omega}{\partial t} + \frac{\partial(\rho u_i \omega)}{\partial x_j} = \frac{\gamma}{\nu_t} - \beta \rho \omega^2 + \frac{\partial}{\partial x_j} (\mu + \sigma_\omega \mu_t) + 2(1 - F_1) \frac{\rho \sigma_\omega 2}{\omega} \frac{\partial k}{\partial x_j} \frac{\partial \omega}{\partial x_j} \quad (3.1.9)$$

For the shear stresses, the Boussinesq approximation is used:

$$\tau_{ij} = 2\mu_t (S_{ij} - \frac{1}{3} \frac{\partial u_k}{\partial x_k} \delta_{ij}) - \frac{2}{3} \rho k \delta_{ij} \quad (3.1.10)$$

P is the production term, defined as

$$P = \tau_{ij} \frac{\partial u_i}{\partial x_j} \quad (3.1.11)$$

And μ_t is the turbulent dynamic viscosity or eddy viscosity defined as

$$\mu_t = \frac{\rho \alpha_1}{\max(\alpha_1 \omega, \Omega F_2)} \quad (3.1.12)$$

A production limiter [14] is usually used in the Production term in the k equation replacing it with the following:

$$P_k = \min(P, 20\beta\omega) \quad (3.1.13)$$

Each of the constants included is a blending between inner and outer constants of the k- ω and k- ϵ models, as follows

$$\phi = F_1 \phi_1 + (1 - F_1) \phi_2 \quad (3.1.14)$$

The rest of the constants are defined as follows

$$F_1 = \tanh(\arg_1^4) \quad (3.1.15)$$

$$\arg_1 = \min[\max(\frac{\sqrt{k}}{\beta \omega d}, \frac{500\nu}{d^2 \omega}), \frac{4\rho \sigma_\omega 2k}{CD_{k\omega} d^2}] \quad (3.1.16)$$

$$CD_{k\omega} = \max(2\rho \sigma_\omega 2 \frac{1}{\omega} \frac{\partial k}{\partial x_j} \frac{\partial \omega}{\partial x_j}, 10^{-20}) \quad (3.1.17)$$

$$F_2 = \tanh(\arg_2^2) \quad (3.1.18)$$

$$F_2 = \max\left(2\frac{\sqrt{k}}{\beta\omega d}, \frac{500\nu}{d^2\omega}\right) \quad (3.1.19)$$

d is the distance from the field point to the nearest wall, $\omega = \sqrt{2W_{ij}W_{ij}}$ is the vorticity magnitude and

$$W_{ij} = \frac{1}{2}\left(\frac{\partial u_i}{\partial x_j} - \frac{\partial u_j}{\partial x_i}\right) \quad (3.1.20)$$

for the rest of the constants the blending is applied between the constants of the $k-\epsilon$ and $k-\omega$ model constants

$$\gamma_1 = \frac{\beta_1}{\beta^*} - \frac{\sigma_{\omega_1}k^2}{\sqrt{\beta^*}} \quad (3.1.21)$$

$$\gamma_2 = \frac{\beta_1}{\beta^*} - \frac{\sigma_{\omega_2}k^2}{\sqrt{\beta^*}} \quad (3.1.22)$$

$$\sigma_{k1} = 0.85, \sigma_{\omega1} = 0.5, \beta_1 = 0.075 \quad (3.1.23)$$

$$\sigma_{k2} = 1, \sigma_{\omega2} = 0.856, \beta_2 = 0.0828 \quad (3.1.24)$$

$$\beta^*0.09, k - 0.41, \alpha_1 = 0, 31 \quad (3.1.25)$$

3.1.2 Boundary Conditions

The original boundary conditions for this solution of this model, recommended by Menter as follows:

$$\frac{U_\infty}{L} < \omega_{farfield} < 10\frac{U_\infty}{L} \quad (3.1.26)$$

$$\omega_{wall} = 10\frac{6\nu}{\beta_1(\Delta d_1)^2} \quad (3.1.27)$$

$$10^{-5}\frac{U_\infty}{L} < k_{farfield} < 0.1\frac{U_\infty}{L} \quad (3.1.28)$$

$$k_{wall} = 0 \quad (3.1.29)$$

3.1.3 The $k-\omega$ SSTm Model

A common variation of the $k-\omega$ SST model comes from the omission of the term $\frac{2}{3}\rho k\delta_{ij}$ in the Boussinesq approximation for τ_{ij} in the momentum equation. The production term is also modified to match the exact expression for incompressible flows as following:

$$P = 2\mu_t S_{ij}^2 \quad (3.1.30)$$

.These 2 modifications create a new model,named the $k-\omega$ SST_m model

3.1.4 The $k-\omega$ SST Model with Vorticity source (SST-V)

The SST-V model [11] is pretty similar to the standard model, but makes use of the vorticity magnitude $\Omega = \sqrt{2W_{ij}W_{ij}}$ for turbulence production. This model is used because Ω is calculated anyways in order to find μ_t . The model equations are the same , with only difference being the production term P in both equations, which is given by the formula:

$$P = \mu_t \Omega^2 - \frac{2}{3}\rho k\delta_{ij} \frac{\partial u_i}{\partial x_j} \quad (3.1.31)$$

Similarly to the standard model, the same production limiter for the k- equation is used.

3.1.5 The $k-\omega$ SST-Vm Model

In a similar approach to the $k-\omega$ SSTm Model, the term $\frac{2}{3}\rho k\delta_{ij}$ is omitted from the energy equation, and the production term takes a new form: $P = \mu_t \Omega^2$. These changes require a new naming convention, thus the SST-Vm model is defined, usually used for hypersonic flow applications.

3.1.6 The $k-\omega$ SST model with Kato-Launder source term(SST-KL, SST-Klm)

In this variation, the vorticity source term is slightly altered to implement the Kato-Launder correction[8], that uses $S\Omega$ instead of Ω^2 . The production term is now given by

$$P = \mu_t S\Omega - \frac{2}{3}\rho k\delta_{ij} \frac{\partial u_i}{\partial x_j} \quad (3.1.32)$$

and the model name changes to SST-KL. Similarly to the previous cases,ignoring the term $\frac{2}{3}\rho k\delta_{ij}$ in the momentum equation and the $\frac{2}{3}\rho k\delta_{ij} \frac{\partial u_i}{\partial x_j}$ from the Production term, the SST-KLm model is defined.

3.2 Boundary Layer-Law of the Wall

The principle of the Wall Function Formulation is the Law of the Wall by Theodore Von Karman. According to the Law of the Wall, there are similarities between different boundary layers, and these can be formulated as following: let u^+ , y^+ be the non-dimensional flow variables (or wall units): $u^+ = \frac{u}{u_\tau}$ and $y^+ = y \frac{u_\tau}{\nu}$, where u_τ is the shear stress velocity, a variable with no physical meaning representing the shear stresses in velocity form:

$$u_\tau = \sqrt{\frac{\tau}{\rho}} \quad (3.2.1)$$

In the following figure, we can see the velocity profile in wall units, and the separation of the sublayer into 3 regions:

the viscous sub-layer ($y^+ < 5$), where the viscous effects are dominant

the buffer layer ($5 < y^+ < 30$), where there is the transition between the viscous and the logarithmic region

and the logarithmic region ($y^+ > 30$), where the velocity profile follows a Logarithmic distribution.

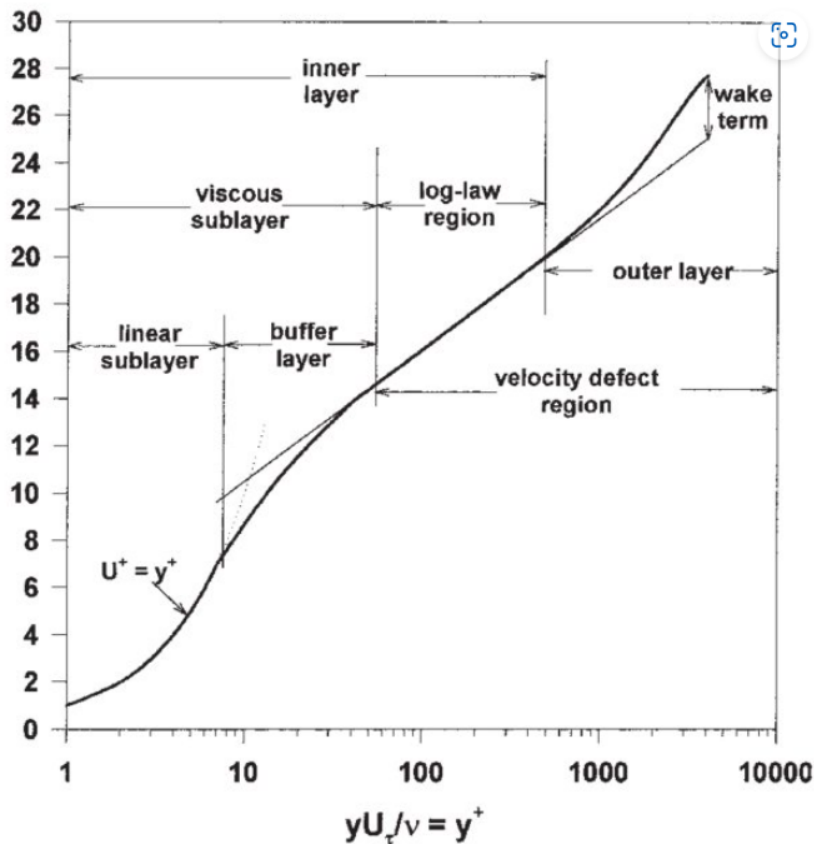


Figure 3.1: Normalised mean velocity profile in a turbulent boundary layer in semi-log coordinates

3.3 Wall Functions

The general idea of the wall function theory is to find a way to bypass the need for a fully resolved near wall mesh. In order to properly solve the near-wall turbulent flow, a fully resolved near-wall mesh is required, and the first point needs to be placed in the viscous sublayer(ideally $y^+ = 1$),requiring large cell numbers and computational resources. Also, increasing the number of cells by a large margin on one part of the mesh only can reduce the quality of the mesh, which can produce numerical problems.

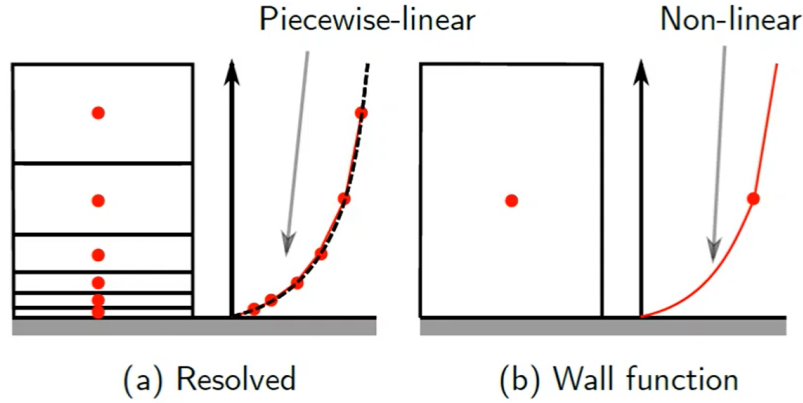


Figure 3.2: Fully Resolved boundary Layer and Wall function Theory

Using the wall function theory, this limitation can be bypassed, and viscous layers of $y^+ > 30$ can be calculated with lower viscous sublayer cell numbers. The Wall function formulation is based on the Law of the Wall, and assuming the first grid point lies in the logarithmic region,the boundary condition for the missing flux in the wall is given[13]:

$$u_\tau = \frac{u}{\frac{1}{\kappa} \log y^+ + C}, \tau_{wall} = \rho u_\tau^2 \quad (3.3.1)$$

where $C=5.5$ and $\kappa = 0.41$ is the von Karman constant In a near wall grid, this assumption is false, and the accuracy of wall functions is reduced, eventually becoming singular as $y^+ \rightarrow 0$.To Avoid this problem a lower limit of y^+ is imposed, and the formulation is altered to

$$u_\tau = \frac{u}{\frac{1}{\kappa} \log \tilde{y}^+ + C}, \tau_{wall} = \rho u_\tau^2, \tilde{y}^+ = \max(y^+, Y_{lim}^+) \quad (3.3.2)$$

where $Y_{lim}^+ = 11.067$ is the point of intersection between the linear and logarithmic profiles, preventing the first grid point from entering the linear area.

3.3.1 Automatic Wall Treatment

Wall functions are not always desirable though, as they neglect the viscous sublayer influence on the flow. In order to solve this problem, the automatic wall treatment method is used. It implies a shift between a viscous sublayer formulation and wall functions, based on grid density. Using the ω equation, which can provide analytical

solutions for both the viscous and logarithmic region solutions for both the viscous sublayer and logarithmic region are obtained:

$$\omega_{visc} = \frac{6\nu}{0.075y^2}, \omega_{log} = \frac{1}{0.3\kappa} \frac{u_\tau}{y} \quad (3.3.3)$$

and with a smooth blending and a reformulation in terms of y^+ :

$$\omega(y^+) = \sqrt{\omega_{visc}(y^+)^2 + \omega_{log}(y^+)^2} \quad (3.3.4)$$

Similarly, the equations for the velocity profile near the wall:

$$u_\tau^{log} = \frac{u}{\frac{1}{\kappa} \log y^+ + C}, u_\tau^{visc} = \frac{u}{y^+} \quad (3.3.5)$$

and with another smooth blending for the velocity equations:

$$u_\tau = [(u_\tau^{visc})^4 + (u_\tau^{log})^4]^{\frac{1}{4}} \quad (3.3.6)$$

3.4 Hull roughness and its effect on ship resistance

In most simulations and flow problem approaches, surfaces are considered to be smooth. However, in real applications, that assumption is always incorrect, especially in the case of ships. In reality the hull surfaces show roughness, and all surface are rough to a degree. Factors that increase roughness usually include the ways of manufacturing the surface, so selecting a method that reduces the possibility of roughness is preferred.

The roughness of a ship is also directly affected by corrosion and paint. Different kinds of paint that are used to prevent corrosion, give different roughness results depending on the sea environment. Fouling is also an important factor, as marine growth directly leads to increased roughness.[18]

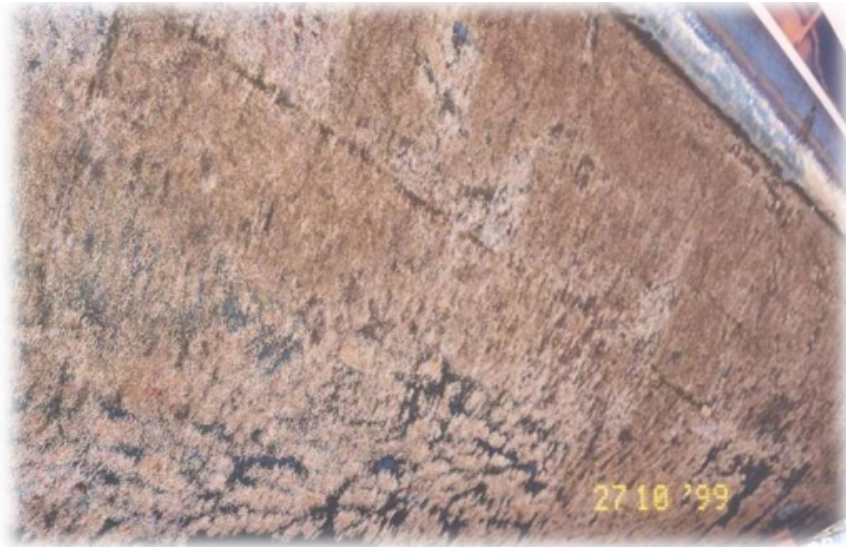


Figure 3.3: fouled hull

In 1933, experiments were conducted by Nikuradse [16] on pipes with sand grains stuck on the surface of the pipes, and examination of the results showed that by increasing the size of the grains (a good measure for the roughness of a surface), the shear stresses on the wall were increased and the velocity profile became broader. Thus, in the case of a ship, the resistance increases, due to the roughness of the surfaces increasing the shear stresses on the surface.

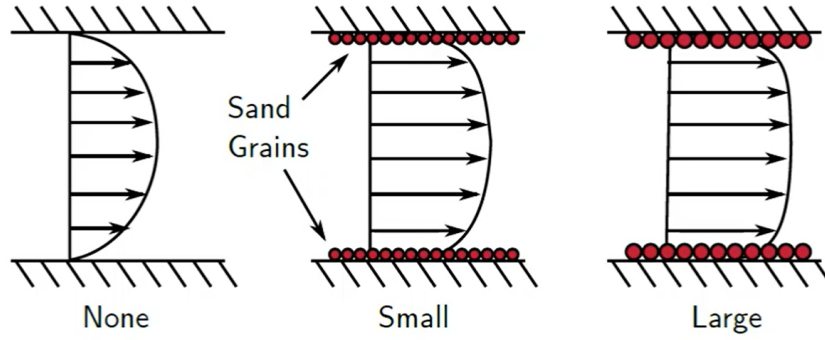


Figure 3.4: effect of sand grains on the velocity profile in a pipe

3.4.1 Wall Functions with roughness corrections

While the wall functions work well in a smooth boundary (smooth surface-smooth ship hull in our case). However, as discussed before, the velocity profile is different when we take into account the wall roughness. The Log-Law in this case is still preserved, but there is a shift in the curve, which can be captured according to Nikuradse by adjusting the y^+ formulation [4].

$$u^+ = \frac{u}{u_t}, u^+ = \frac{1}{\kappa} \log y^+ + C - \Delta u^+ \quad (3.4.1)$$

The velocity shift Δu^+ was found to be related to a wall parameter called the equivalent sand grain height:

$$h_s^+ = \frac{h_s u_\tau}{\nu} \quad (3.4.2)$$

where h_s is the height of the sand grains used in the experiments. The formulation used for the velocity shift is given by Grigson [6]:

$$\Delta u^+ = \frac{1}{\kappa} \log \left(1 + \frac{h_s^+}{\exp(3.25\kappa)} \right) \quad (3.4.3)$$

Chapter 4

Mesh Construction

4.1 The HEXPRESS Software

For the construction of the mesh, the HEXPRESS mesh generating software has been used. HEXPRESS is a software by NUMECA[1]. In this chapter the basic principle of meshing with HEXPRESS, will be briefly discussed.

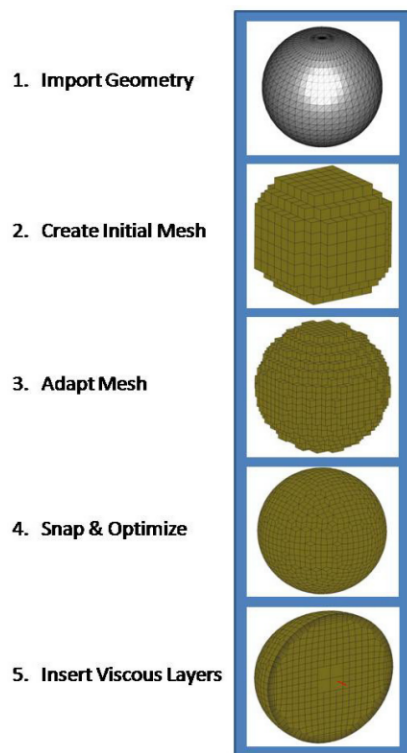


Figure 4.1: The HEXPRESS algorithm

4.2 Initial Mesh

Starting the initial geometry of the hull will be imported on a HEXPRESS project. In order for the simulation to be conducted properly, and the boundary conditions to be assigned correctly, there is a geometry cleanup process, where holes in the ship

geometry are closed. The main deck is also built as a surface, which will be assigned the proper boundary conditions. Initiating the meshing procedure, an initial mesh of 100.000 cells created. The initial mesh is quite coarse, and it does not really affect the end result, as the initial mesh serves as the pivot for the adapt to geometry procedure, where the specific mesh details are captured.

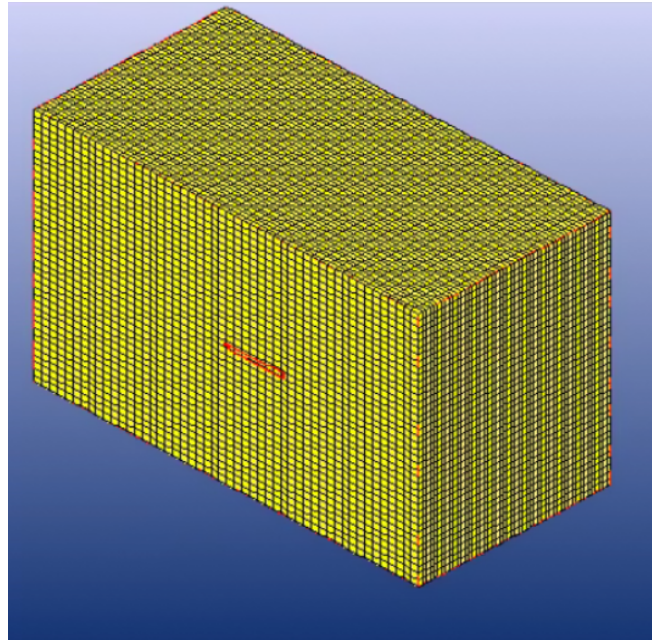


Figure 4.2: Initial mesh of 100.000 cells

4.3 Adapt to Geometry

Moving forwards, the adaptation step initiates. Cells that contain the surface of the hull or curves, will be flagged for refinement, and they are subdivided until certain geometry criterions are met. Geometry criterions can be the curvature of a surface, or curve. Usually the criterion used was the curvature one, as most of the hull surfaces have inherent curvature. Apart from the cells in the hull surface, 2 refinement boxes have been created, will all the cells in them flagged for additional refinements. The first box has the free surface at the middle of the volume. The second box is similar, however smaller, in order for the kelvin wake waves to be captured properly in the simulation. Then the surface/volume intersecting cells are trimmed.

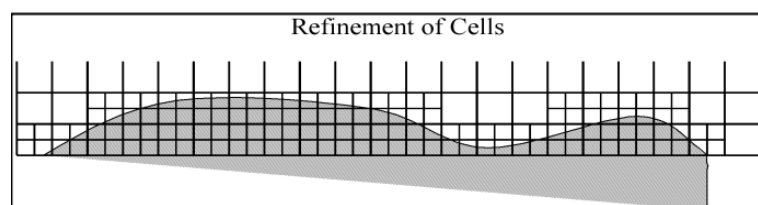


Figure 4.3: cell refinement

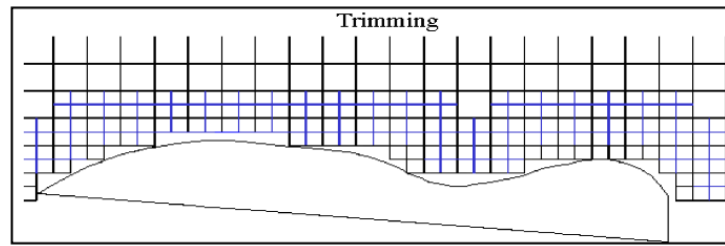


Figure 4.4: cell Trimming

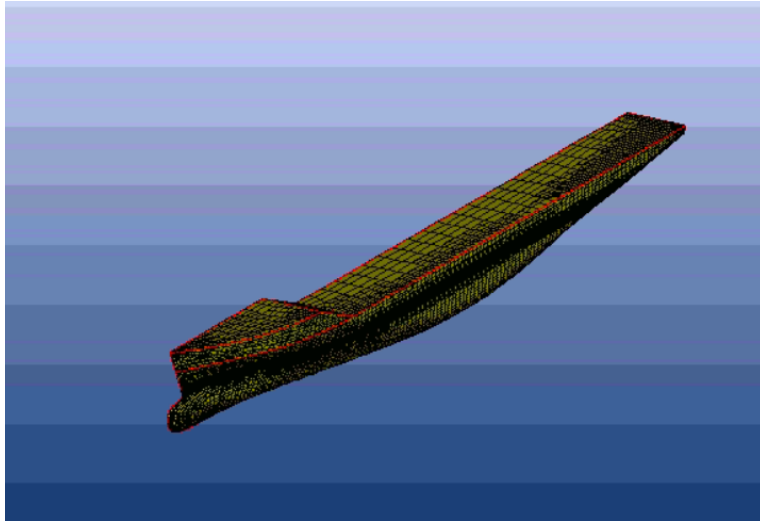


Figure 4.5: Hull surface mesh

4.4 Snap to Geometry-Optimization

The snapping algorithm projects the mesh obtained by trimming on the surface, in order to get a good quality body mesh. Also, any concave, or twisted cells are fixed in the optimization step.

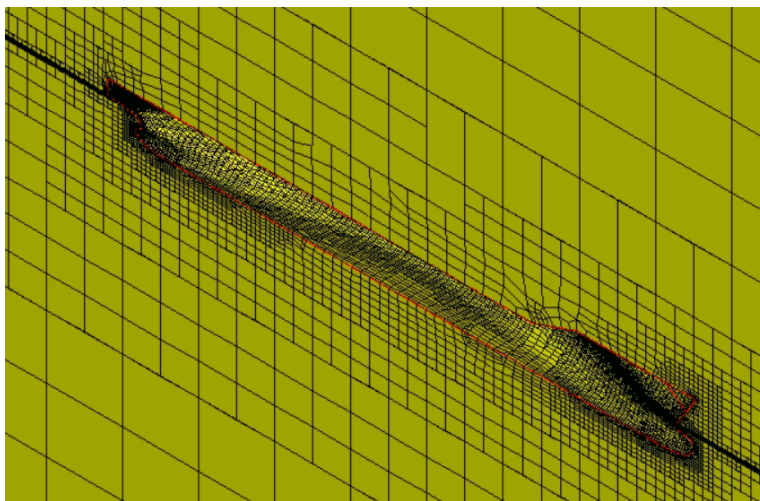


Figure 4.6: Mesh around the hull

4.5 Viscous Layers

Finally, the cells connected to walls, are subdivided once again, inserting the viscous layers of a thickness chosen by the user. This option enables better behaviour of the mesh on the boundary layer, and by choosing a certain y^+ number, the software itself can provide us with an estimated number of layers and a thickness for the first layer (the one connected to the wall). In this study, a minimum y^+ of 30 has been chosen, and a first layer thickness of has been used in all simulations.

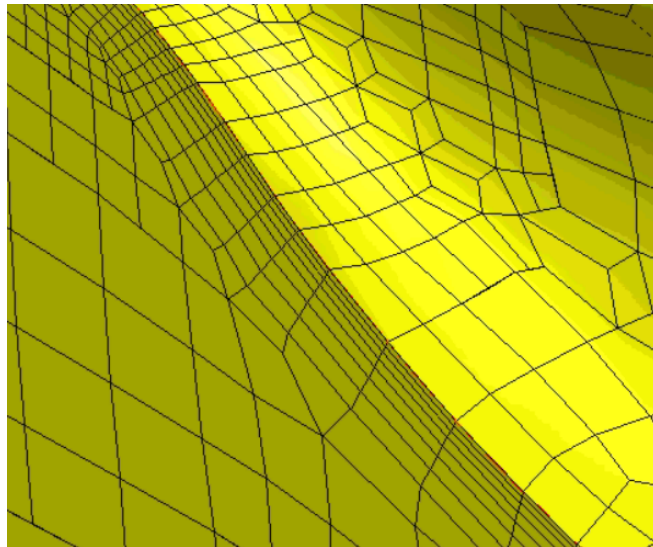


Figure 4.7: Viscous Layers

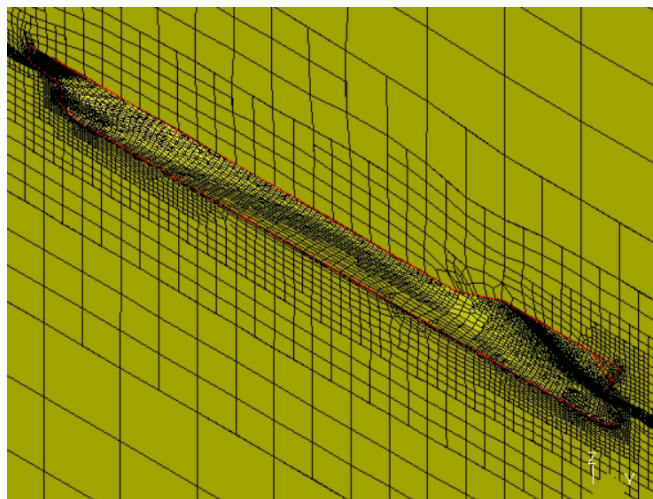


Figure 4.8: Mesh around the hull after Viscous Layer insertion

4.6 Refinement boxes

In order to properly capture the free surface, additional refinement cubes have been created. These cubes are created through python scripts, and are utilised in the adapt to geometry step. The cells inside the volume of the cubes are flagged for additional refinements.

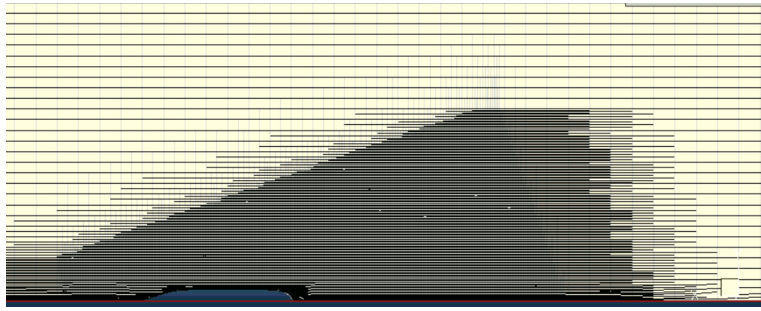


Figure 4.9: Cut plane on the Trim height-Refinement for the Kelvin Wake Pattern

4.7 Boundary Conditions

As stated in previous chapters, in order for the equations to be properly solved, the correct Boundary conditions need to be applied on mesh surfaces. The following boundary conditions have been used:

- Solid: defining the solid surface of the hull-representing the no-slip wall boundary condition.
- Mirror: since the geometry consists of half the hull, a mirror boundary condition is placed on the face of the mesh that coincides with the plane of symmetry of the hull. This condition represents the symmetry boundary condition.
- Exterior: the farfield boundary condition.

Chapter 5

Results

5.1 Hull Geometry

For the study of this thesis, the chosen hull is the Kiso Container Ship(KCS). The KCS Hull is an experimental hull, developed by the KRISO organisation. It is widely used to test the efficiency of CFD methods. Another reason for the choice of the KCS hull is the existence of various experimental results for the NMRI model in particular, which is crucial for the continuation of this work. Using the experimental data, comparisons between the numerical and the experimental simulations can be done, thus validating the results of the simulations. The basic characteristics of both the full scale ship and the chosen model are described in table below.

Table 5.1.1: Hull Geometry

Model	Full-Scale	NMRI
Scale	1	31.599
L_{pp} (m)	230	7.2786
L_{wl} (m)	232.5	7.357
B_{wl} (m)	32.2	1.019
D(m)	19	0.6013
T(m)	10.8	0.3418
Displacement(m^3)	52030	1.649
S without rudder(m^2)	9530	9.5441
C_B	0.651	0.651
C_M	0.985	0.985
V(m/s)	12.36	2.196
F_n	0.26	0.26

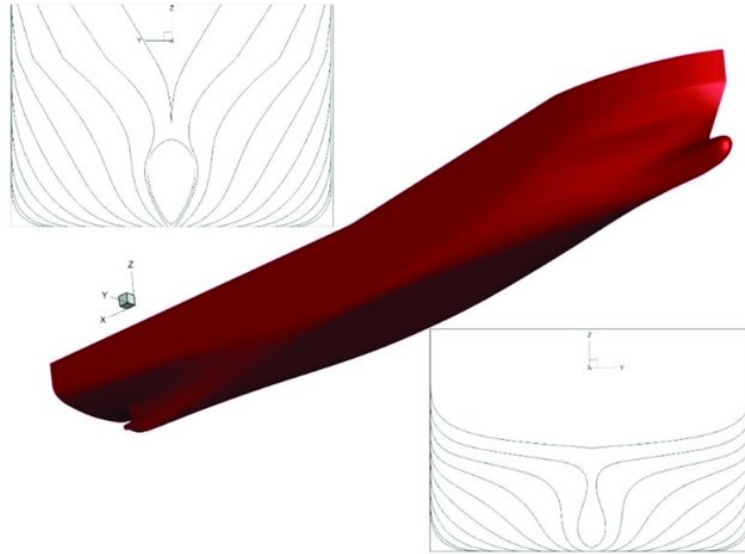


Figure 5.1: The Kriso Container Ship

In accordance to the above, simulations have been conducted on various coarse meshes, with cell number ranging from 254.000 to 1.033.034 cells. Only coarse meshes have been examined, for the purpose of a qualitative assessment of the results without spending tons of computational resources.

In order to facilitate the convergence of the meshes, and a moving grid script was implemented for the ship, with a hyperbolic tangent acceleration in order to reach the desired operational velocity.

A numerical wave tank was also used, in order to absorb the waves radiating from the ship at the ends of the mesh. Also, due to the symmetry of the problem around the horizontal axis, the mesh consisted of only half of the ship. The MaPFlow solver provides us with the forces on the ship on every iteration.

We can use this to plot the resistance of the ship (Body Force on X Axis, F_{BODYx}). Keeping in mind that this resistance consisting of only half of the ship, multiplying the result by 2 we can get the total resistance of the ship at a given timestep.

The total resistance coefficient C_T is calculated as:

$$C_T = \frac{2F_{BODYx}}{0.5\rho V^2 S} \quad (5.1.1)$$

where,

- ρ is the water density,
- S the wetted surface of the hull, and
- V the operation velocity of the hull.

A graph of the behavior of the body force x is presented:

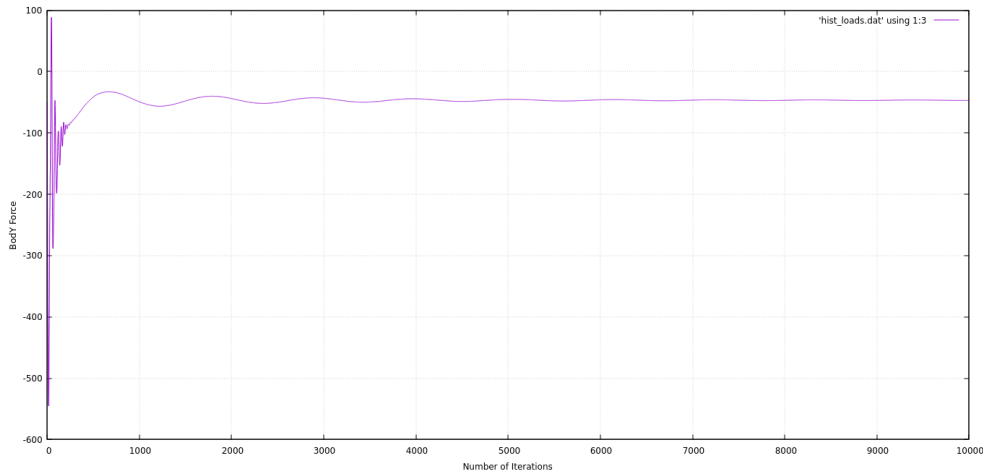


Figure 5.2: Force on X-Axis(Resistance)-Time iterations

As shown, the resistance has many oscillations at the beginning of the simulation. In order to find the resistance coefficient a mean value of the oscillation due to the wave is calculated after the solution converges.

The accuracy of the results is validated by the deviation of the mesh results from the experimental results [9]:

$$E\% = \frac{C_{T_S} - C_{T_D}}{C_{T_D}} 100\% \quad (5.1.2)$$

where the indexes S and D represent the results from the simulation and the experimental results. Also, the convergence of the mesh is validated using the mesh deviation:

$$\epsilon\% = \frac{C_{T_2} - C_{T_1}}{C_{T_1}} 100\% \quad (5.1.3)$$

where the index 2 and 1 represent the results of the current mesh used and the previous, more coarse mesh .

Table 5.1.2: Mesh convergence

Simulation	$C_T \star 10^3$	E	ϵ
Experiment	3.711		
Mesh #1(274.497 cells)	4.52	22,00%	
Mesh#2(612.058 cells)	3.98	7.2%	13,00%
Mesh#3 (1.033.034 cells)	3.83	3.2%	3.7%

Also, simulations with the roughness correction discussed in previous chapters has also been conducted. The grain heights chosen for the simulation are the standard values for hull roughness, of 120 μm for a new ship. Due to fouling and deterioration, this value typically increases to 300-400 μm , so another simulation for 300 μm has also been examined.

5.2 $k - \omega$ SST simulation results

As shown from the results of the chapter above convergence has been achieved, and the results of the final mesh can be examined. The quality of the results, is directly related to the fact that most of the cells in the mesh, consist of the hull surface and the kelvin wake refinement box. As such, the simulation results are expected to be less accurate the further we are from the hull surface, and have higher accuracy close to the hull. In order to visualise the results, the ParaView software has been used. Below some results of post processing of Mesh #3 are shown.

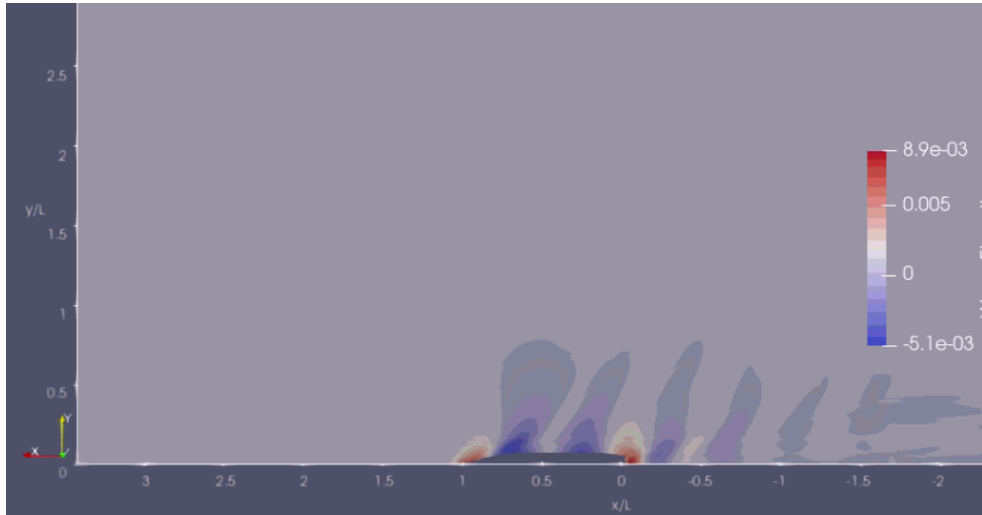


Figure 5.3: Wave Elevation- $k-\omega$ SST model

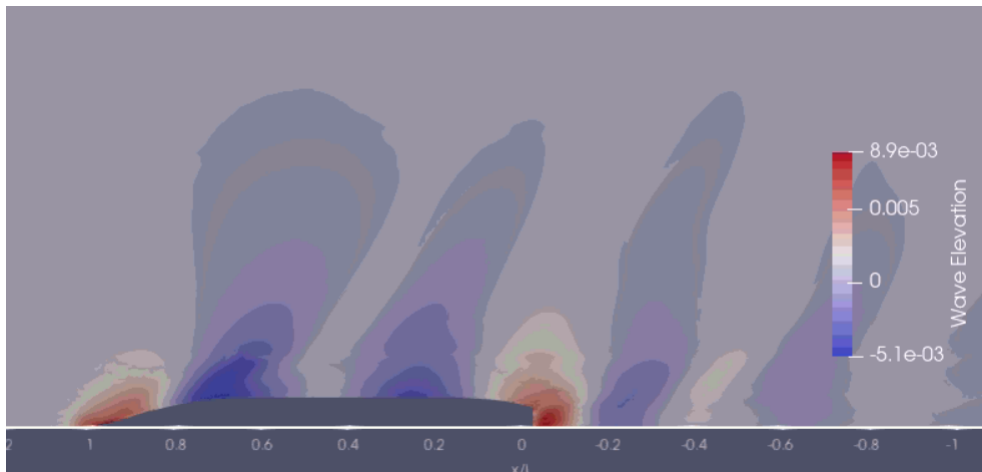


Figure 5.4: Wave elevation close to the hull

In the images above, the free surface elevation close to the hull is presented. As expected, the wave patterns are more accurate close to the hull. As the mesh cells move away from the hull, we get a less accurate wave profile. The results close to the hull need validation in order for the mesh to be suitable for use in the rest of the simulations. A way to verify the accuracy of the results is to examine wave elevation sections, also known as wave cuts close to the hull, and compare the given results to the experimental ones by Kim.

Also, having experimental data for the wave elevation on the hull, where the best result is expected to appear, we can compare the experimental data on the wave pattern on the hull.

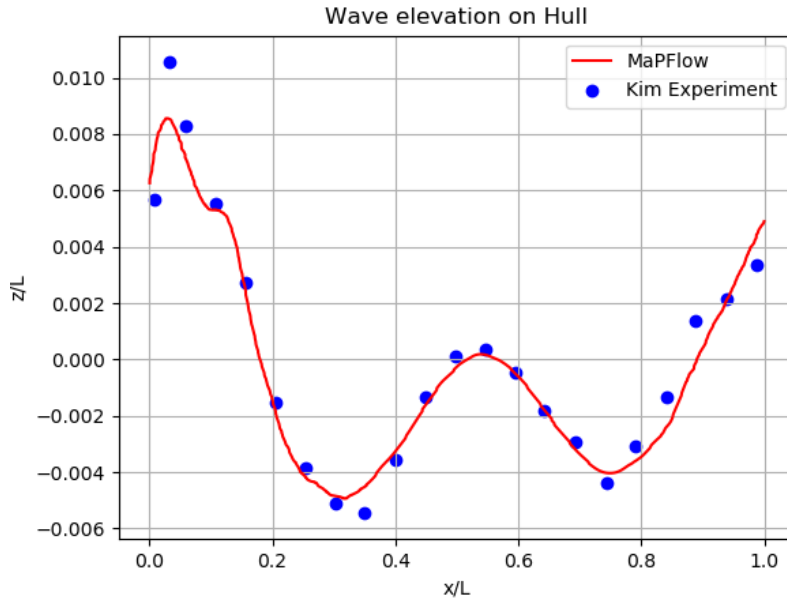


Figure 5.5: Wave elevation on Hull surface-MaPFlow and Experiment

From the comparison of the data for the wave elevation around the hull, the simulation shows expected results. Some peaks of the wave pattern appear to have slight difference in value, but this can be expected from a simulation on a coarse mesh. Now, 2 wave cuts will be examined.

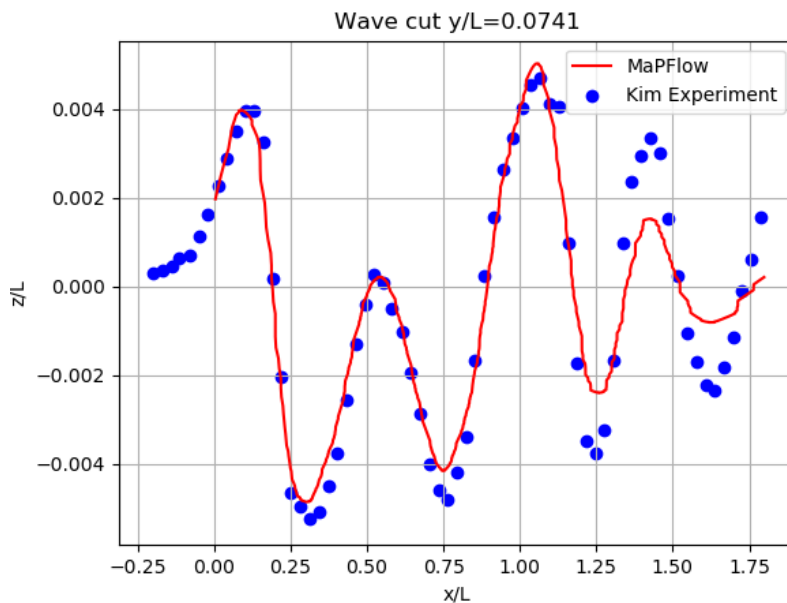


Figure 5.6: Wave cut $y/L=0.0741$ -MaPFlow and Experiment

Comparing the simulation data for the first wave cut, the comparison changes. The

results of the simulation match the experimental data when examining the range of $x/L = [0.1, 2.5]$. This is happening because of the additional mesh refinements for the kelvin wake pattern. Moving further away from this range, the results deviate from the experiment. This is expected, because of the use of a coarse mesh, and utilising most of the refinement resources for the hull and the Kelvin Wake. Moving further away from the hull in the Y-Axis, an even less accurate result is expected on a wave cut for a higher y/L .

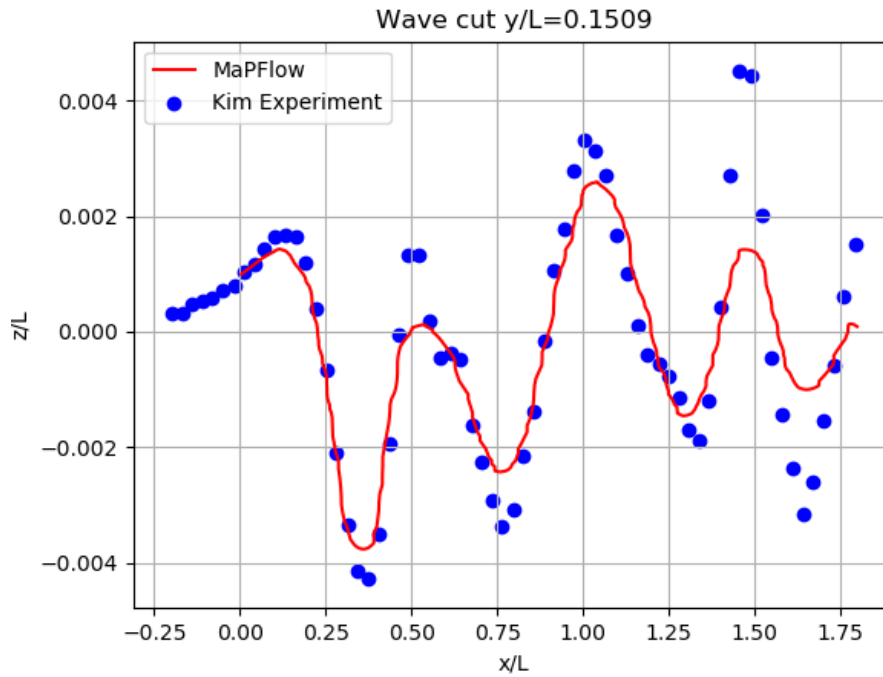


Figure 5.7: Wave cut $y/L=0.1509$ -MaPFlow and Experiment

Looking at another wave cut of a higher y/L even in the range of $x/L = [0, 1.25]$ we see different results on the wave pattern. This result is expected, and acceptable. This result shows the limitations coarse meshes, and while the resistance results shown before were accurate enough for further examination of the mesh, the coarse mesh limitations are still present. However, while the values deviate from the experiment, the mesh is still considered valid for use, as the main focus of this study is the resistance. The free surface elevation is satisfying enough, and it is appropriate for the comparison of the rest of the models.

Another way to verify this is to look at the behaviour of the flow close to the hull. Specifically, for the velocities at the y - z plane a contour of the y - z velocity profile on the propeller plane ($x = 0.1671$) is presented below. The reasoning for this is the examination of the fluid velocity close to the surface, using only the y and z parts of the velocity, similarly to a 2-dimensional problem.

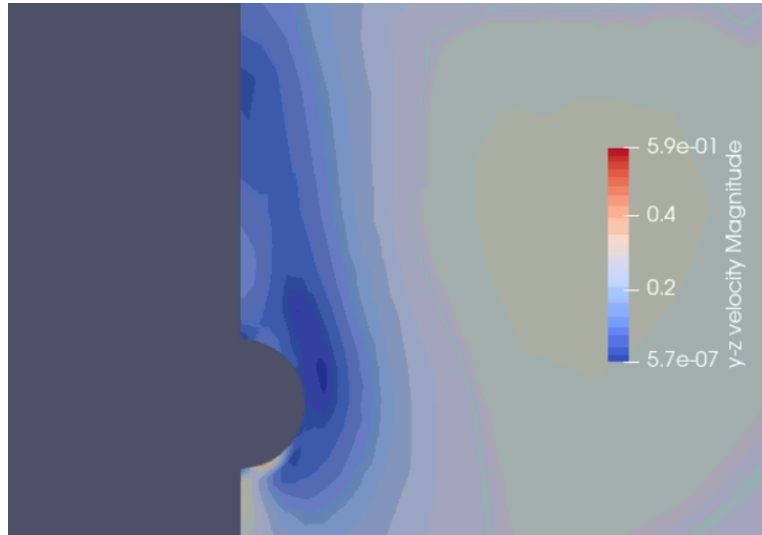


Figure 5.8: y-z Velocity contour

The result is satisfying enough, showing us a good simulation of the boundary layer around the propeller. Also, the mean axial velocity (V_x/V_s) will be examined in the same position.

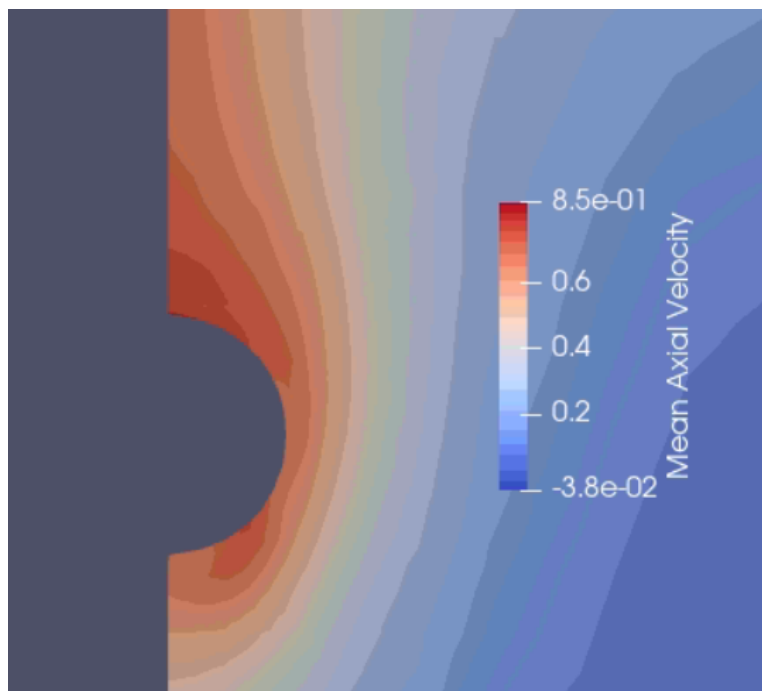


Figure 5.9: Mean Axial Velocity Contour

Concluding the examination of the $k-\omega$ SST model, the conclusion that the mesh used is satisfying emerges. These results, alongside the satisfying resistance value are enough for us to be able to use this mesh, in order to compare the $k-\omega$ SST variations.

In the following chapters, wave elevation and velocity profile will be examined, where all the resistance results will also be discussed. In all the following simulations, the wave cut results were the same, a result expected from the use of the same coarse mesh of 1.033.034 cells.

5.3 $k - \omega$ SSTm simulation results

In the case of the SSTm model, the results are expected to be almost identical to the $k-\omega$ SST model. This expectation lies to the origin of the model changes being incompressible flows. The change in the production term is true for incompressible flows, such as the flow around a hull. This is validated, not only from the wave cuts, but also from the free surface elevation:

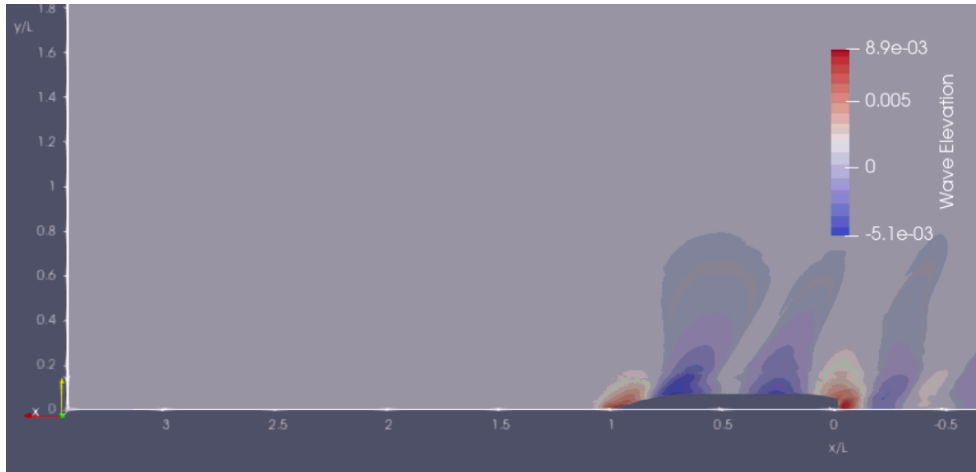


Figure 5.10: Wave Elevation- $k-\omega$ SSTm model

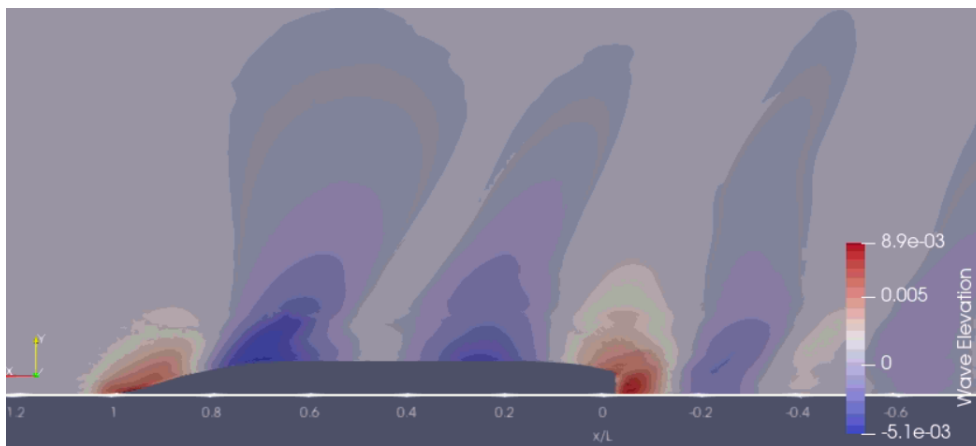


Figure 5.11: Wave elevation close to the hull

The hypothesis is proven correct. The results are identical to a point where differences are not shown in the wave elevation contours. The results of the $y-z$ velocity profiles and mean axial velocity profiles are also expected to be identical

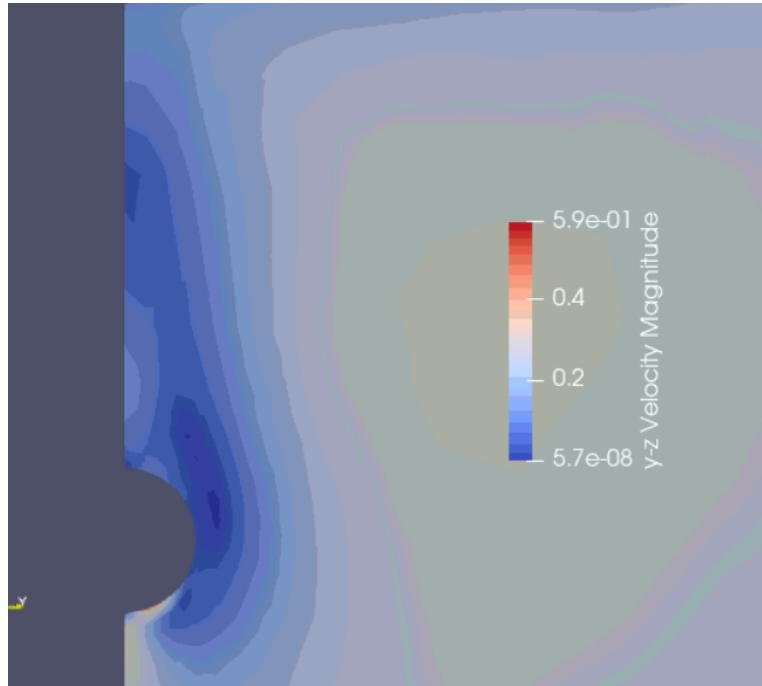


Figure 5.12: y-z Velocity contour

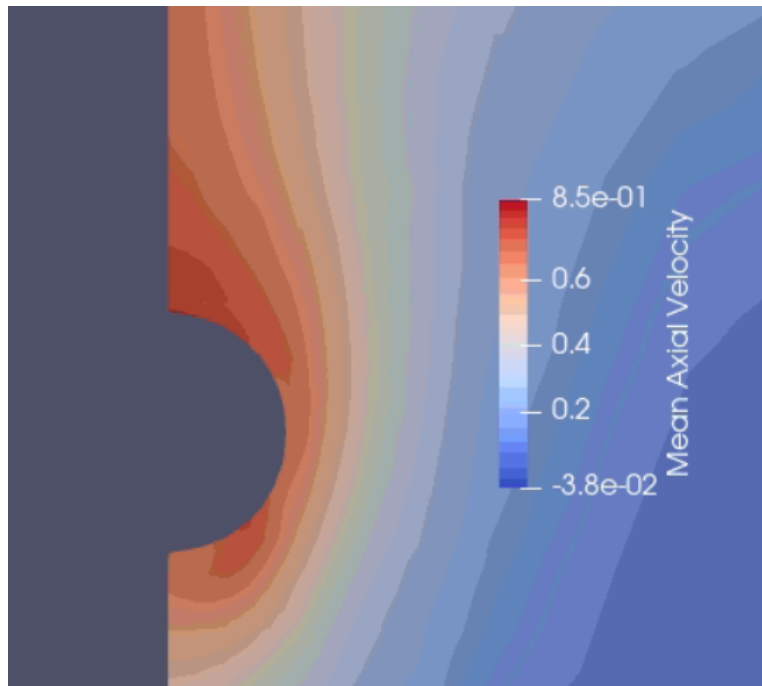


Figure 5.13: Mean Axial Velocity Contour

Confirming the initial theory hypothesis, that the standard SST, and SSTm models are identical for incompressible flows. As such this conclusion can also be drawn for the rest of the models and their ‘m’ counterparts. So the simulations proceeded using only the ‘m’ models, as the results are expected to also be identical between SST-V and SST-Vm, and SST-KL and STT-KLm respectively.

5.4 $k - \omega SST - V_m$ simulation results

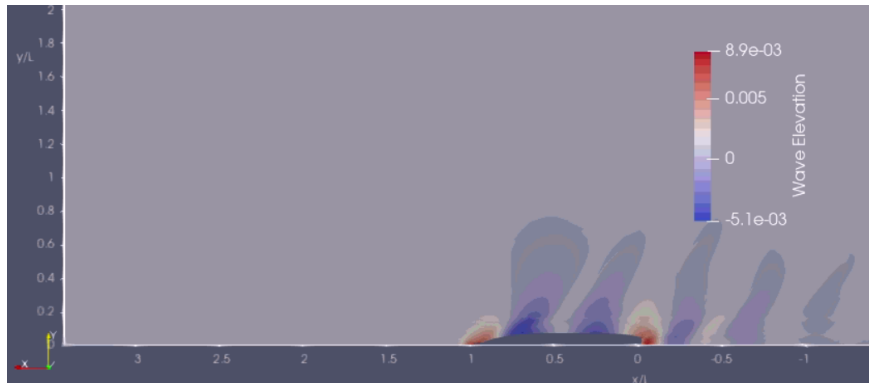


Figure 5.14: Wave Elevation- $k-\omega$ SST V_m model

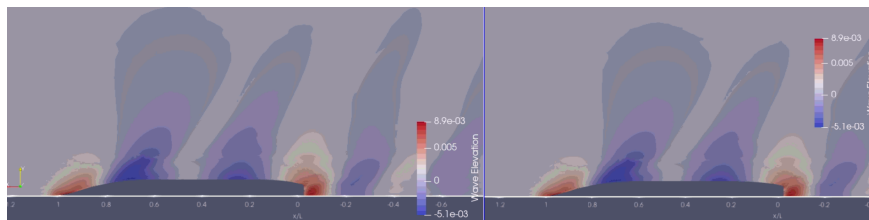


Figure 5.15: Wave elevation close to hull: $k-\omega$ SSTm(left) and SST- V_m (right)

Comparing the free surface elevation of the 2 models, we can see almost identical results, with some very minor differences in the hull. This is also confirmed from the wave elevation around the hull graphs, with similar matching.

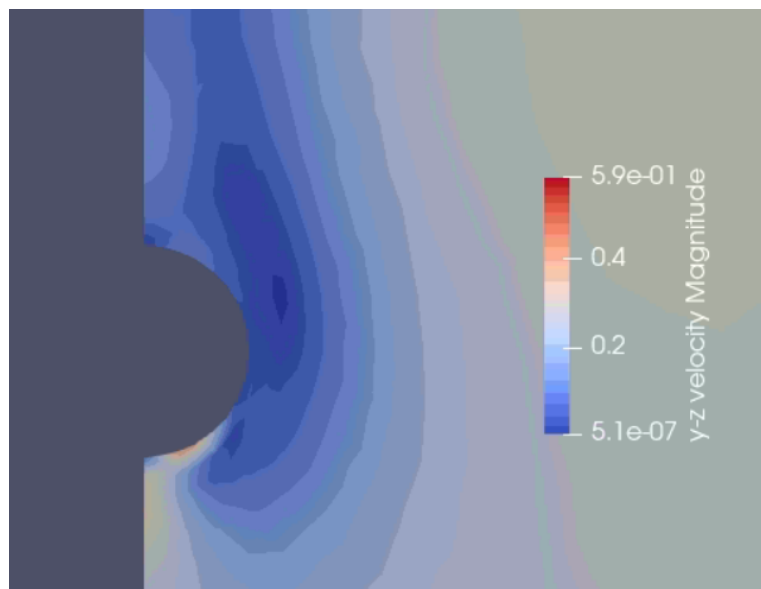


Figure 5.16: $y-z$ Velocity Contour

The values of the $y-z$ velocity change very little, considering the fact that we are talking numbers in the 10^{-7} order. Thus, the results are practically the same. The mean axial velocity contour shown below also gives the same result.

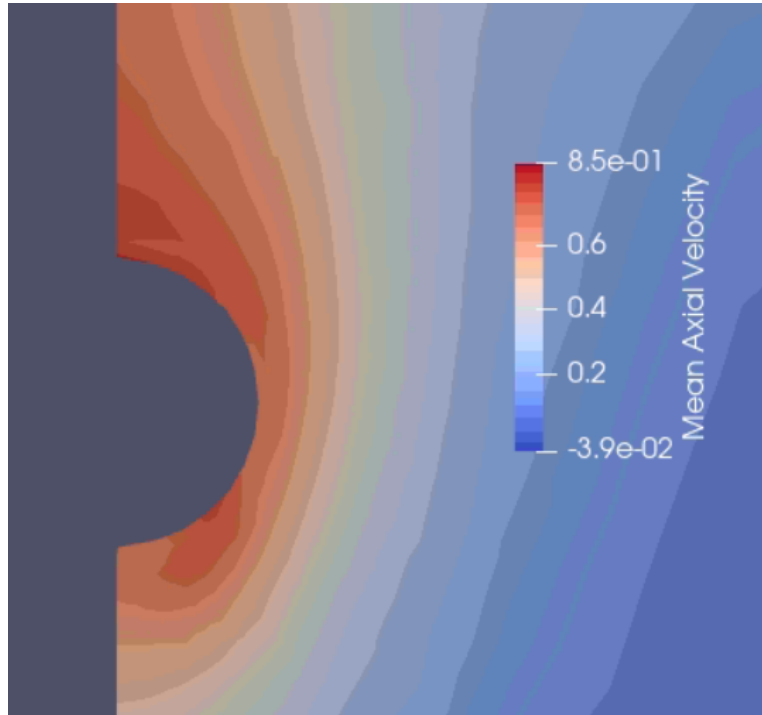
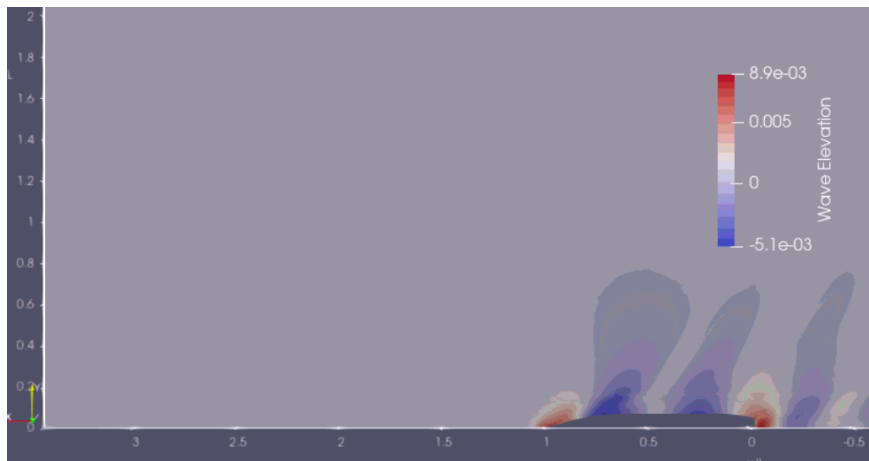
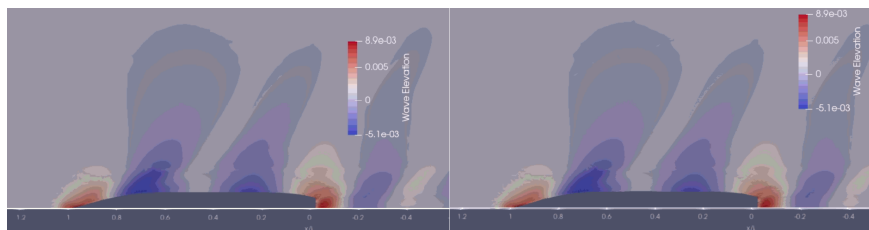


Figure 5.17: Mean Axial Velocity Contour

5.5 $k - \omega$ SST-Klm simulation results

Figure 5.18: Wave Elevation- $k-\omega$ SST-KLm modelFigure 5.19: Wave elevation close to hull: $k-\omega$ SST-Vm(left) and SST-KLm(right)

Comparing the Klm model to the Vm Model, once again we little to no significant difference on the wave elevation. The 2 models are very similar, with the Kato-Launder corrections affecting the vaues of the free surface elevation negligibly

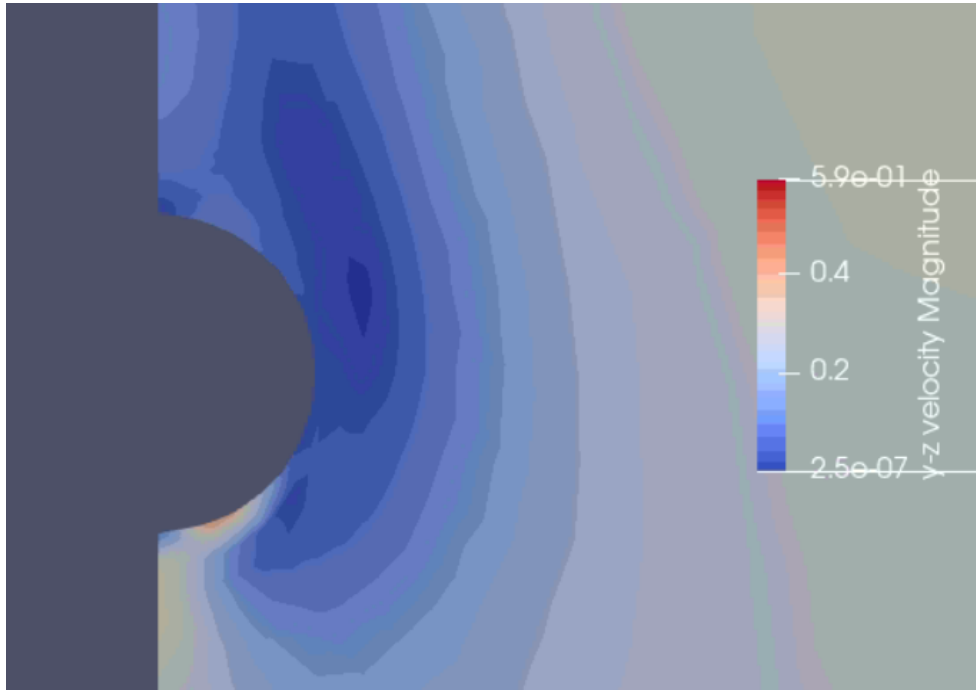


Figure 5.20: y-z Velocity Contour

Regarding to the velocity profile in the propeller plane, see smaller velocity values can be seen, nearly half, however, when regarding the velocity values, the difference once again seems negligible, considering numbers of order 10^{-7} .

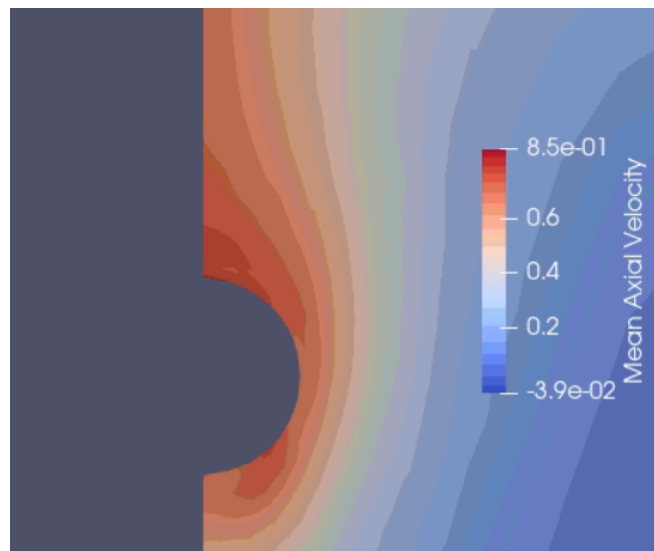


Figure 5.21: Mean Axial Velocity Contour

5.6 Roughness correction results ($h_s=120\mu\text{m}$)

As discussed above, 2 different roughness cases will be examined: first is the case of a mean sand grain height of $120\mu\text{m}$, the standard value for hull roughness.

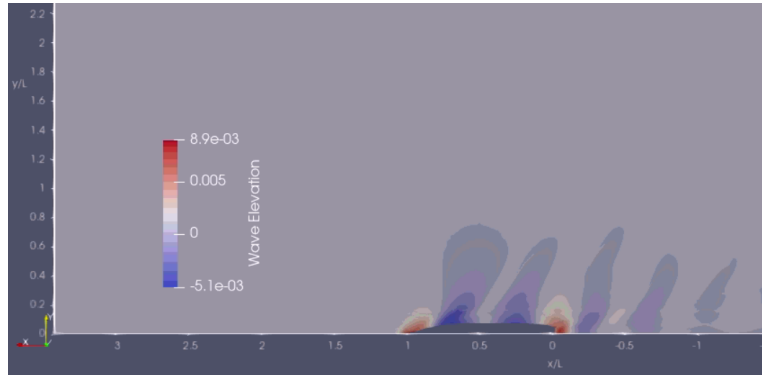


Figure 5.22: Wave Elevation:k- ω SST model With roughness correction($h_s = 120\mu\text{m}$)

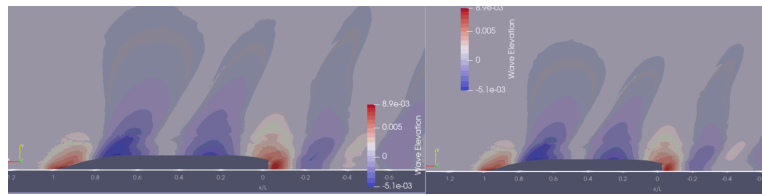


Figure 5.23: Wave elevation close to hull-k- ω SST model Without roughness correction(left)- With roughness correction(right)

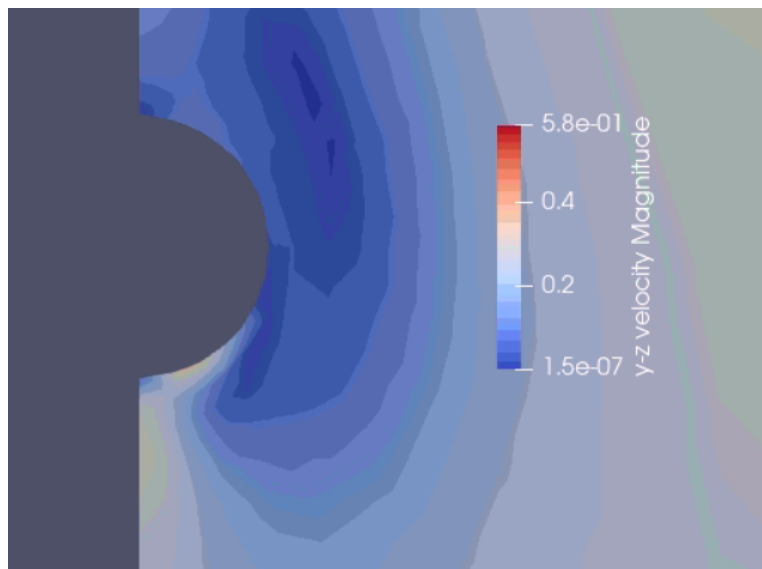


Figure 5.24: y-z Velocity Contour

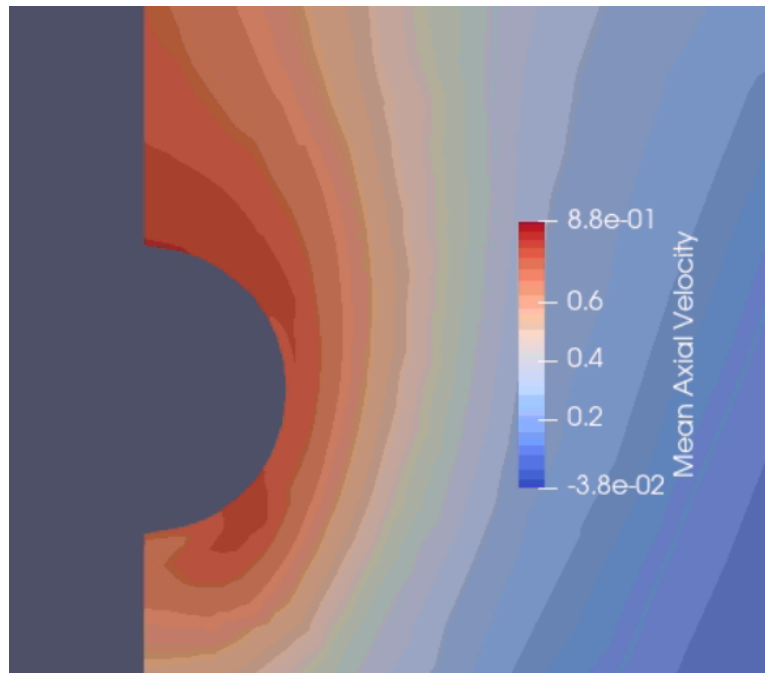
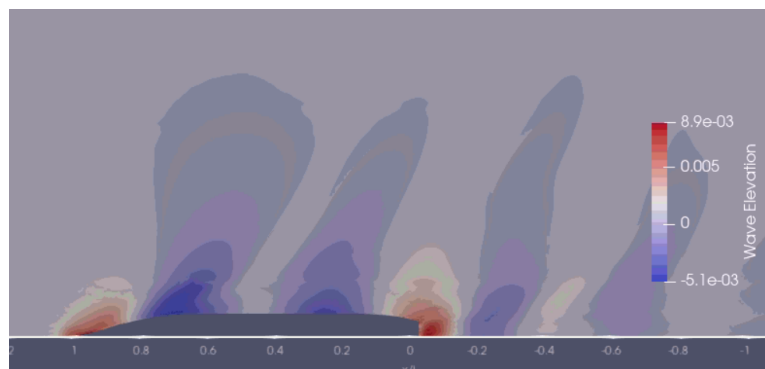


Figure 5.25: Mean Axial Velocity Contour

Comparison between the standard model and the model with roughness correction shows some differences in the wave pattern behind the hull. This result is expected considering the rough surfaces increase friction and velocities close to the surface, Also, the maximum values of the mean axial velocity increase close to the hull, result expected considering Nikuradse's experiments. The results of a second simulation, with $h_s = 300\mu m$ are also shown below.

5.7 Roughness correction results($h_s=300\mu m$)

Figure 5.26: Wave Elevation:k- ω SST model With roughness correction($h_s = 300\mu m$)

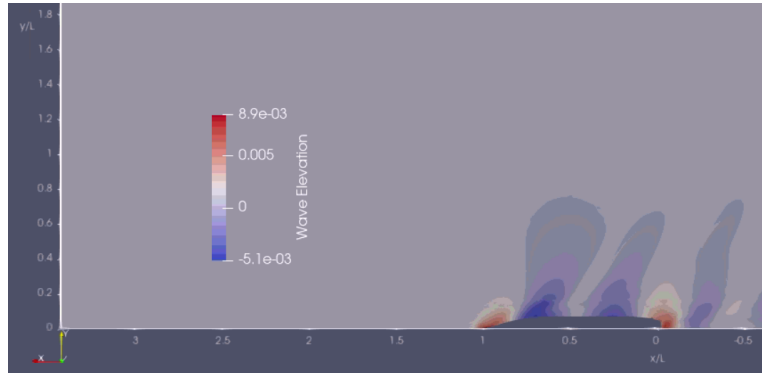


Figure 5.27: Wave Elevation close to hull: $h_s = 120\mu m$ (left) $h_s = 300\mu m$ (right)

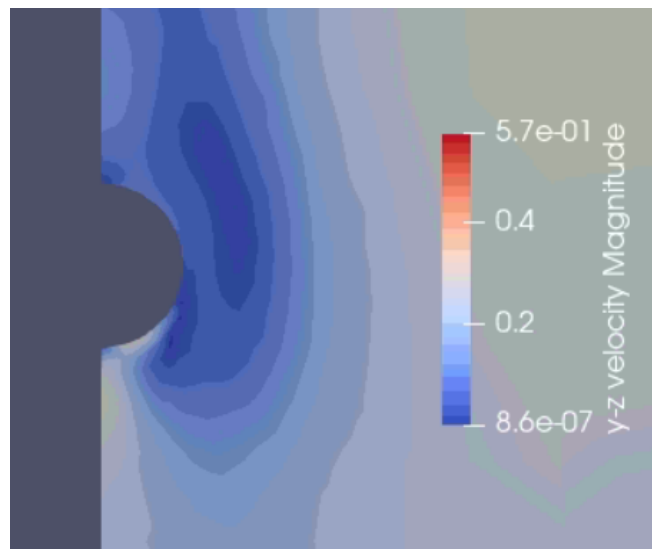


Figure 5.28: y-z Velocity Contour

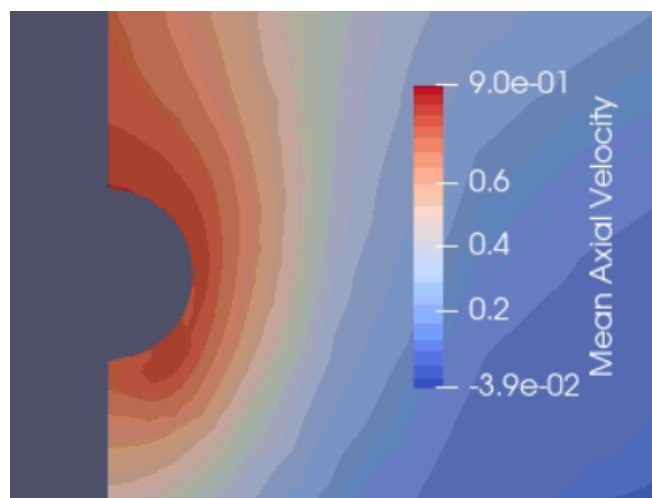


Figure 5.29: Mean Axial Velocity Contour

5.8 Resistance Results

After comparing the free surface elevation and velocity profile values, a comparison of the resistance coefficients. This is the most important aspect of this thesis, as the value of the resistance coefficient, and the value of the resistance, directly linked to the coefficient, is the In the following table, the values of the resistance coefficient, calculated in the same way as the initial simulation, is presented:

Table 5.8.1: comparison of the resistance coefficients of the simulations

Simulation	$C_T 10^3$	% Deviation from SST
Kim experiment	3.711	
SST	3.8316	
SSTm	3.8316	0%
SST-Vm	3.8528	0.5%
SST-KLm	3.883	1.3%
SST-roughness correction(120 microns)	4.500	17.4%
SST-roughness correction(300 microns)	4.963	29.5%

As we can conclude from this table, the values of the resistance coefficient change very slightly, on the second decimal digit. The values of the resistance change very slightly when varying by model. The numerical values of the standard SST model and SSTm model are exactly identical. This was expected from the theory of the SSTm model correction being exact for incompressible flows.

Comparison between the SSTm and SST-Vm models, a very slight increase of 0.5 % is observed. This increase. Although very small in numerical value, the difference does exist, and so the SST or SSTm models are give slightly better results in the case of a hull.

The Kato-Launder correction gives an even higher difference in resistance of 1.3% . It is the higher difference that can be seen in the non-roughness models. Although still on the smaller side of numbers, the Kato-Launder correction gives worse results. Thus, it should not be used if the aim of the simulation is the maximum accuracy of the resistance.

On a general note, though, the differences are on a pretty small scale. Thus, depending on the need for a normal accuracy order for a ship designer, all of the model variations are deemed suitable for use. Comparing the standard SST model with the SST model with the roughness correction we can see an increase of 17% in the resistance coefficient. This in the case of sand grain height of 120 microns. Increasing the sand grain height to 300 microns, the increase in resistance goes up to 29.5% . This type of difference is normal in the case of a fully rough hull surface, which is what the wall function correction implies. In real applications, not every part of the hull has that type of roughness, and the roughness is different in every hull surface, resulting in lower resistance values than the case of a fully rough hull.

Concluding remarks and recommendation for future research

The purpose of this thesis was threefold. The first aim was to look at the resistance problem utilizing the MaPFlow solver. The goal was to obtain accurate results using low computational resources, using wall functions and the $k-\omega$ SST model. One of the main purposes of wall functions is to reduce the computational cost, as a fully resolved boundary layer would require much more computational cells.

The second aim, was to compare the turbulence model results. In this work, only a few variations of the standard Menter Shear Stress Transport model were used. While computing the resistance coefficients and wave elevation profiles, the variations showed that changes in the production term of the turbulence models does not change the total resistance results a lot, and neither does for the wave elevation. This is only in the case of a ship problem, as discussed before, as in different fields these models give different results, and each model is preferred for different applications. In the case of a ship resistance problem, the major conclusion is that while the standard model gives the best approximation, the approximations of the model variations are close enough to be considered for use, and the difference between them will not be of importance for the researcher, as there was no difference higher than 1.5%.

The third part was hull roughness. The study in this case was only for the standard model, as it was the model with the best numerical result. Using the simple sand grain height correction, a non-negligible numerical difference in hull resistance coefficients was found. Increasing the roughness only increased this difference. Keeping in mind that this experiment was for a fully rough hull, the combination of turbulence modeling with roughness gave good results.

On future research upon the topic of turbulence modeling in ship resistance, the first step forward would be the comparison of the rest of the turbulence models. That is, comparing the results of three and seven equation models, to examine if there can be an even better result for the case of ship resistance.

Another further research case could be the omission of wall functions alongside the various turbulence models. While wall function are good in reducing computational resources, and synergize well with turbulence modeling, if the researcher has the computational resources, a fully resolved grid could be examined, for all the cases discussed in this study and the rest of the turbulence models. On the computational resource scope, even more detailed meshes could be used in different problems, in order to further validate the similarities between the turbulence models.

Finally, regarding roughness, one could examine the differences in turbulence model results using different roughness models, or examine the effect of roughness model in the case of other turbulence models. This can include both other variations of the $k-\omega$ SST model, or others. Examining whether the corrections are valid with the rest of the

models, or use other corrections to the models themselves, rather than the wall function application.

Bibliography

- [1] Hexpress user manual. <https://www.scribd.com/document/363823438/261664278-UserManual-HEXPRESS-pdf>.
- [2] Kcs geometry and conditions. [:http://www.simman2008.dk/KCS/kcs_geometry.htm](http://www.simman2008.dk/KCS/kcs_geometry.htm).
- [3] A.Dermatis. *Numerical modelling of regular and irregular breaking waves using a coupled artificial compressibility method*. 2022.
- [4] F. Chedevergne. *Analytical wall function including roughness corrections*. International Journal of Heat and Fluid Flow, 2018.
- [5] A. J. Chorin. *A numerical method for solving incompressible viscous flow problems*. Comput. Phys., 135:118–125, 1967.
- [6] C. Grigson. *Drag losses of new ships caused by hull finish*. Journal of Ship Research 36, (1992).
- [7] C. Hirt and B. Nichols. *Volume of Fluid (VOF) Method for dynamics of free boundaries*. J. Comput. Phys., 1981.
- [8] M. Kato and B. E Launder. *The Modelling of Turbulent Flow Around Stationary and Vibrating Square Cylinders*. 9th Symposium on Turbulent Shear Flows, 1993.
- [9] Takanori Hino. Frederick Stern. Lars Larsson. Michel Visonneau. Nobuyuki Hirata .Jin Kim. *Numerical Ship Hydrodynamics An Assessment of the Tokyo 2015 Workshop*. Springer, 2015.
- [10] B. P. Leonard. *d. Simple high accuracy resolution program for convective modelling of discontinuities*. Int. J. Numer. Meth. Fluids, 1988.
- [11] F. R. Menter. *Improved Two-Equation k-omega Turbulence Models for Aerodynamic Flows*. NASA TM 103975, 1992.
- [12] F. R Menter. *Two-Equation Eddy-Viscosity Turbulence Models for Engineering Applications*. AIAA Journal, Vol. 32, No. 8, 1994.
- [13] F. R. Menter. *Elements of industrial heat transfer predictions*. 16th BRAZILIAN CONGRESS OF MECHANICAL ENGINEERING, 2001.
- [14] F. R Menter. *Zonal Two Equation k-omega Turbulence Models for Aerodynamic Flows*. AIAA Paper 93-2906., July 1993.

-
- [15] S. Muzaferija and M. Peric. *Computation of free-surface flows using interface tracking and interface capturing methods*. Non linear water waves interaction, 1999.
- [16] J. Nikuradse. *Law of Flow in Rough Pipes*. Technical Memorandum 1292, National Advisory Committee for Aeronautics, 1950.
- [17] R.; Abdel-Maksoud Perić. *Reliable damping of free-surface waves in numerical simulations*. Ship Technol. Res, 2016.
- [18] G. Politis. *Αντίσταση και Πρόωση πλοίου*. National Technical University of Athens, 2019.
- [19] P. L. Roe. *Approximate riemann solvers, parameter vectors and difference schemes*. J. Comput. Phys., 43:357–372, 1981.
- [20] S. Tsaggaris. *Μηχανική των Ρευστών*. ΕΚΔΟΣΕΙΣ ΣΥΜΕΩΝ, 2005.